Title

COMPARISON OF THREE-JET AND RADIATIVE TWO-JET EVENTS IN ELECTRON-POSITRON ANNIHILATION AT 29 GeV

Author

Sheldon, P.D.

Publication Date

1986-11-01

Lawrence Berkeley Laboratory
UNIVERSITY OF CALIFORNIA

Physics Division

Comparison of Three-Jet and Radiative Two-Jet Events in Electron-Positron Annihilation at 29 GeV

P.D. Sheldon
(Ph.D. Thesis)

November 1986

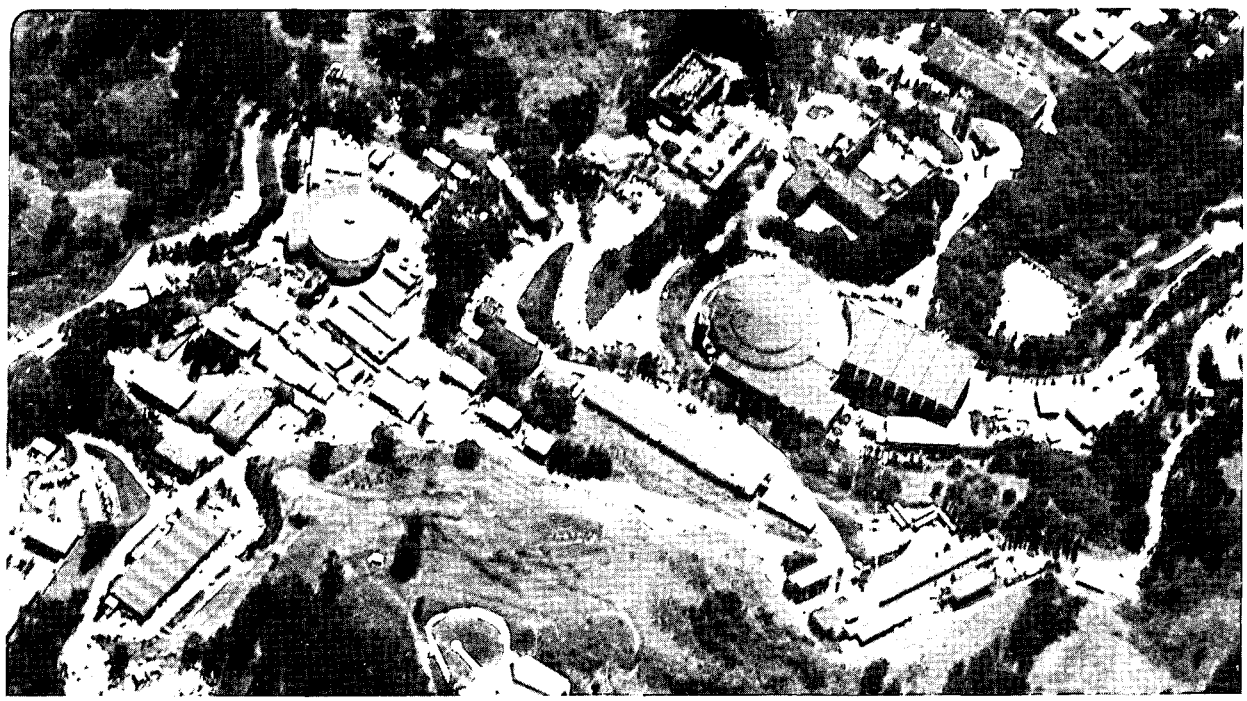

Prepared for the U.S. Department of Energy under Contract DE-AC03-76SF00098

DISCLAIMER

LBL-22525

Comparison of Three-Jet and Radiative Two-Jet Events in Electron-Positron Annihilation at 29 GeV

Paul Douglas Sheldon

(Ph.D. Thesis)

Lawrence Berkeley Laboratory

University of California

Berkeley, California 94720

November 1986

This work was supported by the Director, Office of Energy Research, Office of High Energy and Nuclear Physics, Division of High Energy Physics of the U.S. Department of Energy under Contract Number DE-AC03-76SF00098.

Comparison of Three-Jet and Radiative Two-Jet Events in Electron-Positron Annihilation at 29 GeV

Paul Douglas Sheldon

ABSTRACT

By comparing *3-jet* ($e^+e^- \rightarrow q\bar{q}g$) and radiative *2-jet* ($e^+e^- \rightarrow q\bar{q}\gamma$) events from electron-positron annihilation, we have studied the local and global effects of the presence of a hard bremsstrahlung gluon in hadronic events. Detector and event selection efficiencies and biases affect these two kinds of events almost equally because they have very similar kinematics and topologies. Accurate comparisons of $q\bar{q}g$ and $q\bar{q}\gamma$ events can therefore be made.

Globally, we observe a depletion of hadrons in $q\bar{q}g$ events relative to $q\bar{q}\gamma$ events on the opposite side of the event plane from the gluon, in the angular region between the q and $\bar{q}$ jets. This depletion is shown to be in agreement with the predictions of Quantum Chromodynamics (QCD). The existence of this effect demonstrates that the presence of a gluon significantly alters the color forces and hence the fragmentation process in hadronic events.

We also use these $q\bar{q}\gamma$ and $q\bar{q}g$ events to compare low energy (4.5 GeV) gluon and quark jets. Our data indicate that gluon jets have softer x_p distributions than quark jets, while the transverse momentum distributions of these two types of jets are identical within our errors. Although we are unable to determine if the multiplicities of gluon (n_g) and quark (n_q) jets are different, the ratio $n_g/n_q = 9/4$ predicted asymptotically in QCD would not be consistent with our data.

to my parents:

who unfailingly encouraged, prodded, directed and believed
— but never required

"Few things are harder to put up with than the annoyance of a good example."

— Mark Twain, *Pudd'nhead Wilson's Calender*, 1894

Acknowledgements

In my tenure with them, I have benefited greatly from the "good examples" of the members of the Mark II Collaboration. It would be impossible to list all of their many contributions to my training as a physicist, but some have been so significant that they must be acknowledged. First and foremost, I would like to thank my thesis advisor, George Trilling. His conscientiousness, selfless energy, and excellence as a physicist have provided me with a superlative role-model. I am also deeply indebted to Gerson Goldhaber, who gave a young and very green undergraduate a chance to participate in a "real" physics experiment, and to Andy Lankford, Don Briggs and Heidi Schellman, who made that early experience so enjoyable, rewarding and educational.

For helping me to understand and interpret much of the analysis presented in this dissertation, I owe much to Alfred Petersen. Stimulating and informative conversations with Werner Hofmann, Jonathan Dorfan, Bryan Webber, Torbjörn Sjöstrand and Gail Hanson have also been very helpful.

To my parents, who nurtured and humored my dreams and aspirations all these years, and to all of my family, who have always acted as if my success was a foregone conclusion, I am deeply grateful.

Finally and most importantly, I adoringly acknowledge the many contributions (both tangible and intangible) of my wife, Sue. Her wit, kindness, compassion, intelligence and joy are a constant reward to all who know and love her.

Table of Contents

Chapter 1. Introduction

Although Quantum Chromodynamics (QCD) has been the accepted theory of strong interactions for over ten years, only modest progress has been made in testing its basic features. For example, very little is known about the gluon, which according to QCD is the messenger (or "gauge") particle of the strong force. The gluon is expected to have a non-zero strong-interaction charge and therefore have self-interactions. This "non-abelian" nature of QCD has not yet been verified.

High energy electron-positron (e^+e^-) collisions provide a good environment for studying QCD because events containing strongly interacting particles (hadrons) are produced via a simple mechanism. This mechanism is shown in Fig. 1.1(b): an electron and positron annihilate, creating a virtual photon from which a quark (q) and anti-quark ($\bar{q}$) materialize. The strong force between the quarks causes them to fragment into hadrons, which tend to cluster in two "jets" around the directions of the original q and $\bar{q}$. Evidence (albeit circumstantial) for the existence of the gluon was provided in 1979 when events with three hadron jets were observed in e^+e^- annihilations at the PETRA storage ring in Hamburg, Germany.[1] In the framework of QCD, such events are produced when either the initial q or $\bar{q}$ radiates a hard non-colinear gluon ($e^+e^- \rightarrow q\bar{q}g$, see Fig. 1.2(a)). The gluon then fragments into a separate jet. This interpretation was strengthened when it was shown that the jet angular distributions in these events were consistent with a gluon spin of one.[2]

Several groups have used these *3-jet* events to study the impact of gluon bremsstrahlung on particle production in e^+e^- hadronic events. Gluons are expected to have both local and global effects. Locally, gluons should fragment differently than quarks, producing jets with different hadron momentum and multiplicity distributions.[3,4] Comparisons of quark and gluon jets are complicated by difficulties in identifying gluon jets and by the necessity of comparing equal energy jets, but differences have been observed.[5–7] Globally, recent QCD calculations[8] predict a de-

pletion of particles in the angular region between the q and $\bar{q}$ jets relative to the number of particles in the region between the q and g jets or the region between the $\bar{q}$ and g jets. Although there is evidence for this effect,[9,10] it has only recently[11,12] been observed directly. One of these direct observations[11] will be described here.

In this dissertation, we present a new method for studying the effects of gluon bremsstrahlung which relies on a detailed comparison of *3-jet* events and radiative *2-jet* events ($e^+e^- \to q\bar{q}\gamma$, see Figs. 1.4(a)–(b)). Accurate comparisons are possible because these two event types have very similar topologies and kinematics, and therefore have nearly identical systematic errors. Since the hard gluons of *3-jet* ($q\bar{q}g$) events are replaced by photons in radiative *2-jet* ($q\bar{q}\gamma$) events, global differences in particle production caused by hard gluon emission can be observed directly. In addition, radiative *2-jet* events provide a source of known quark jets which can be compared with equal energy gluon and quark jets from *3-jet* events. Hence, this method allows us to study the properties of the gluon with small systematic uncertainties and without having to rely heavily on Monte Carlo models.

1.1 Hadronic Event Production in e^+e^- Annihilation

Before discussing the effects of gluon bremsstrahlung in more detail, we review the theory and phenomenology of hadronic event production in e^+e^- annihilation, with emphasis on the formation of *3-jet* and radiative *2-jet* events.

1.1.1 The Parton Model

In the quark-parton model, hadronic events are produced in e^+e^- annihilation through the creation of a quark (q) anti-quark ($\bar{q}$) pair

$$e^+e^- \to \gamma^* \to q\bar{q} \tag{1.1}$$

in a manner analogous to muon pair production

$$e^+e^- \to \gamma^* \to \mu^+\mu^- \,. \tag{1.2}$$

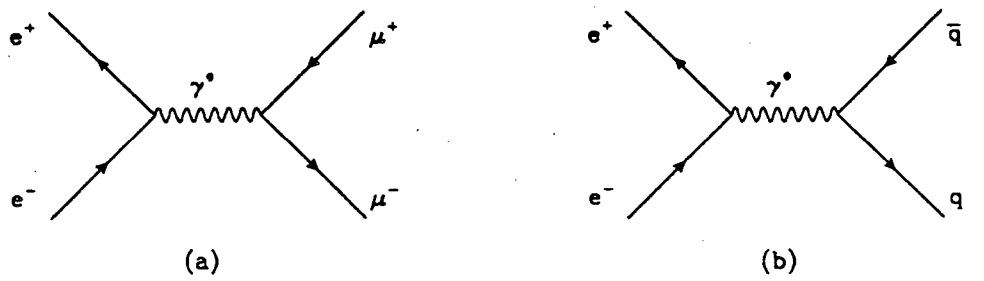

Figure 1.1 *Feynman diagrams for (a) muon pair production and for (b) parton model hadron production in e^+e^- annihilation.*

Feynman diagrams are shown in Fig. 1.1 for both of these reactions, which are pure Quantum Electrodynamical (QED) processes. Both the initial and final-state particles have a point-like coupling to the virtual annihilation photon. Assuming that quarks have spin $\frac{1}{2}$, the cross-section for reaction (1.1) is related to that for (1.2) by

$$\begin{aligned} \sigma_{q\bar{q}} &= e_q^2 \, \sigma_{\mu\mu} = e_q^2 \, \frac{4\pi\alpha^2}{3s} \\ &= e_q^2 \, \frac{87.6nb}{s} \qquad (s \text{ in } (\text{GeV})^2) \end{aligned} \tag{1.3}$$

where e_q is the charge of the quark in units of the charge of the electron, α is the fine structure constant and $s = (E_{cm})^2$ is the squared center-of-mass energy of the reaction. This relation holds when s is well above the threshold for $q\bar{q}$ production and is not close to any $q\bar{q}$ resonances.

There is good evidence for the existence of five flavors of quark, and a sixth flavor is expected theoretically. Table 1.1 gives the charges and effective masses of these quarks. Assuming that the $q\bar{q}$ pairs in reaction (1.1) produce hadrons with unit probability, the total cross-section for hadronic event production in the parton model is

$$\sigma_0 = 3 \sum_{i=1}^{N_f} e_{q_i}^2 \, \sigma_{\mu\mu} = R \, \sigma_{\mu\mu} \tag{1.4}$$

where N_f is the number of quark flavors that can be produced and R is defined as the ratio of the hadronic and muon pair production cross-sections. Using Table 1.1, we find that $R = 3.67$ at $s = (29 \text{ GeV})^2$. The factor of 3 in (1.4) comes from the

Table 1.1 *The charges (in units of electron charge) and effective masses of quarks known or thought to exist.*

Quark	*Charge*	*Effective Mass*
up (u)	+2/3	0.3 GeV/c^2
down (d)	−1/3	0.3 GeV/c^2
strange (s)	−1/3	0.5 GeV/c^2
charm (c)	+2/3	1.5 GeV/c^2
bottom (b)	−1/3	5.0 GeV/c^2
top (t)	+2/3	>20 GeV/c^2

three possible color charges of quarks (color charge is the strong force equivalent of electric charge). Measurements of R agree with the predictions of (1.4) to within 10% over a wide range of s (see, for example, page 13 of Ref. 13). By assuming that hadronic events are produced via a point-like coupling of $q\bar{q}$ pairs to the annihilation photon, the parton model is able to explain the observation that R is constant over a wide range of s, and is able to predict the approximate value of R.

The agreement between (1.4) and measurements of R implies that the mechanism of quark hadronization is sufficiently soft not to interfere with the hard scattering process which produces the quarks. If the production of hadrons is a soft process, then the hadrons should roughly retain the original quark directions, and at high enough energies they should cluster around the quark directions in "jets". Jets of hadrons in e^+e^- annihilation were first observed by Hanson *et al.*[14] at $E_{cm} = 6$ GeV.

1.1.2 QCD Corrections to the Parton Model

Although in approximate agreement with the data, the R predicted by (1.4) is systematically low. The average of several measurements[15] of R in the energy range 30 GeV $< E_{cm} <$ 37 GeV gives $R = 3.96 \pm 0.10$. The discrepancy between this

measurement and (1.4) can be corrected by using QCD to improve the predictions of the parton model. QCD is modeled after the gauge theory of electromagnetic interactions, QED. The fundamental strongly interacting particles are a triplet of colored, spin-$\frac{1}{2}$ quarks and an octet of massless, spin-1 gluons. Mesons are $q\bar{q}$ bound states, and baryons qqq bound states. Three color charges are necessary so that baryons made of three otherwise identical quarks satisfy the Pauli exclusion principle. The group structure of QCD (SU(3)) is more complex than QED (U(1)), which has only one interaction charge. Because of this complex structure, the vector bosons of the theory (gluons) carry a color and an anti-color charge and have self-interactions. There are strong indications that color is confined in QCD, so that the only observable states are colorless bound states of quarks and gluons. This is because the renormalized coupling constant, α_s, is a function of the four-momentum squared (Q^2) of the interaction of interest: at large Q^2 (short distances) α_s is small, while at small Q^2 (long distances) α_s becomes large and confining. This behavior of the coupling constant is known as asymptotic freedom, and it is due directly to the self-interactions of the gluon. It is asymptotic freedom that makes the parton model possible: in hard processes like (1.1) ($Q^2 = s \simeq 25 - 2500$ (GeV)^2) α_s is small, the quarks are produced quasi-free, and QCD perturbation theory is valid. For the subsequent relatively soft process of hadron formation ($Q^2 \simeq m^2_{proton} \simeq 1$ (GeV)^2), however, perturbation theory cannot be used. Detailed descriptions of QCD can be found in the review articles listed in Ref. 16.

The first-order QCD corrections to the parton model hadronic cross-section are shown in Fig. 1.2. Gluon bremsstrahlung (Fig. 1.2(a)) produces $q\bar{q}g$ final states, and diagrams with virtual gluons (Fig. 1.2(b)) contribute to the lowest-order process of $q\bar{q}$ production (Fig. 1.1(b)). Using the scaled parton energies

$$x_i \equiv 2\,E_i/\sqrt{s}$$

$$x_1 + x_2 + x_3 = 2$$

$$0 \leq x_i \leq 1$$

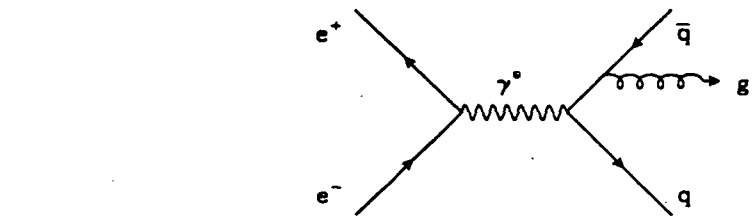

(a)

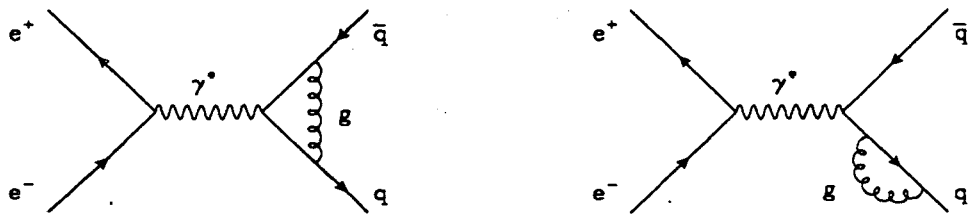

(b)

Figure 1.2 *Feynman diagrams for the order α_s contributions to the process $e^+e^- \rightarrow$ hadrons: (a) gluon emission ($e^+e^- \rightarrow q\bar{q}g$) diagrams, (b) corrections to $e^+e^- \rightarrow q\bar{q}$.*

the lowest-order differential cross-section for $q\bar{q}g$ production is[17]

$$\frac{d^2\sigma_{q\bar{q}g}}{dx_1\,dx_2} = \frac{2\alpha_s}{3\pi}\,\sigma_0\,\left[\frac{x_1^2+x_2^2}{(1-x_1)(1-x_2)}\right] \tag{1.5}$$

where x_1 and x_2 are the scaled energies of the quark and anti-quark and σ_0 is the lowest-order cross-section given in (1.4). This cross-section diverges if x_1 or $x_2 \rightarrow 1$, which occurs when the gluon energy $x_3 \rightarrow 0$ or when the angle between the gluon and either the quark or anti-quark $\theta_{qg} \rightarrow 0$. Therefore, the integrated cross-section $\sigma_{q\bar{q}g}$ is infinite. However, combining the zeroth and first-order diagrams (Figs. 1.1(b) and 1.2) the total hadronic cross-section

$$\sigma_1 = \sigma_{q\bar{q}} + \sigma_{q\bar{q}g} = \left(1+\frac{\alpha_s}{\pi}\right)\sigma_0 \tag{1.6}$$

is finite;[18] because the divergences in (1.5) are cancelled by the divergences from the virtual correction diagrams shown in Fig. 1.2(b). The QCD-improved calculation

of R, then, is

$$R = \left(1 + \frac{\alpha_s}{\pi}\right) 3 \sum_{i=1}^{N} e_{q_i}^2 \, .$$

At $E_{cm} = 29$ GeV, $\alpha_s/\pi \simeq 1/20$, so $\sigma_1 = 1.05\,\sigma_0$ and $R = 3.85$. This value of R is in better agreement with experiment.

At high enough energies, the emitted gluon in $q\bar{q}g$ events will often produce a separate, visible jet. However, when $x_3 \to 0$ or $\theta_{qg} \to 0$, only *2-jet* structure is visible and a $q\bar{q}g$ event is indistinguishable from a $q\bar{q}$ event. This suggests a method for avoiding the divergences of (1.5). By using a resolution criterion to define "observable" events, a finite $q\bar{q}g$ or *3-jet* cross-section can be obtained. One such criterion is to require that the squared invariant mass

$$y_{ij} = \frac{(\mathrm{p}_i + \mathrm{p}_j)^2}{s} = \frac{m_{ij}^2}{s} \tag{1.7}$$

of any two partons i and j satisfy $y_{ij} \geq y_{min}$. Then

$$\begin{aligned} \sigma^{3\text{-}jet} &= \int\limits_{y_{ij} \geq y_{min}} dx_1\, dx_2\, \frac{d^2\sigma_{q\bar{q}g}}{dx_1\, dx_2} \\ \sigma^{2\text{-}jet} &= \sigma_1 - \sigma^{3\text{-}jet} \, . \end{aligned} \tag{1.8}$$

The *2-jet* cross-section has contributions from σ_0, the irresolvable part of $\sigma_{q\bar{q}g}$, and the virtual corrections of Fig. 1.2(b). A good value to use for y_{min} is the energy at which *2-jet* events were first resolved

$$y_{min} \cdot s = (6\ \mathrm{GeV})^2 \, . \tag{1.9}$$

With this cut at $E_{cm} = 29$ GeV, where $\alpha_s/\pi \simeq 1/20$, (1.8) gives[13]

$$\begin{aligned} \sigma^{3\text{-}jet}/\sigma_1 &= 0.3 \\ \sigma^{2\text{-}jet}/\sigma_1 &= 0.7 \, . \end{aligned} \tag{1.10}$$

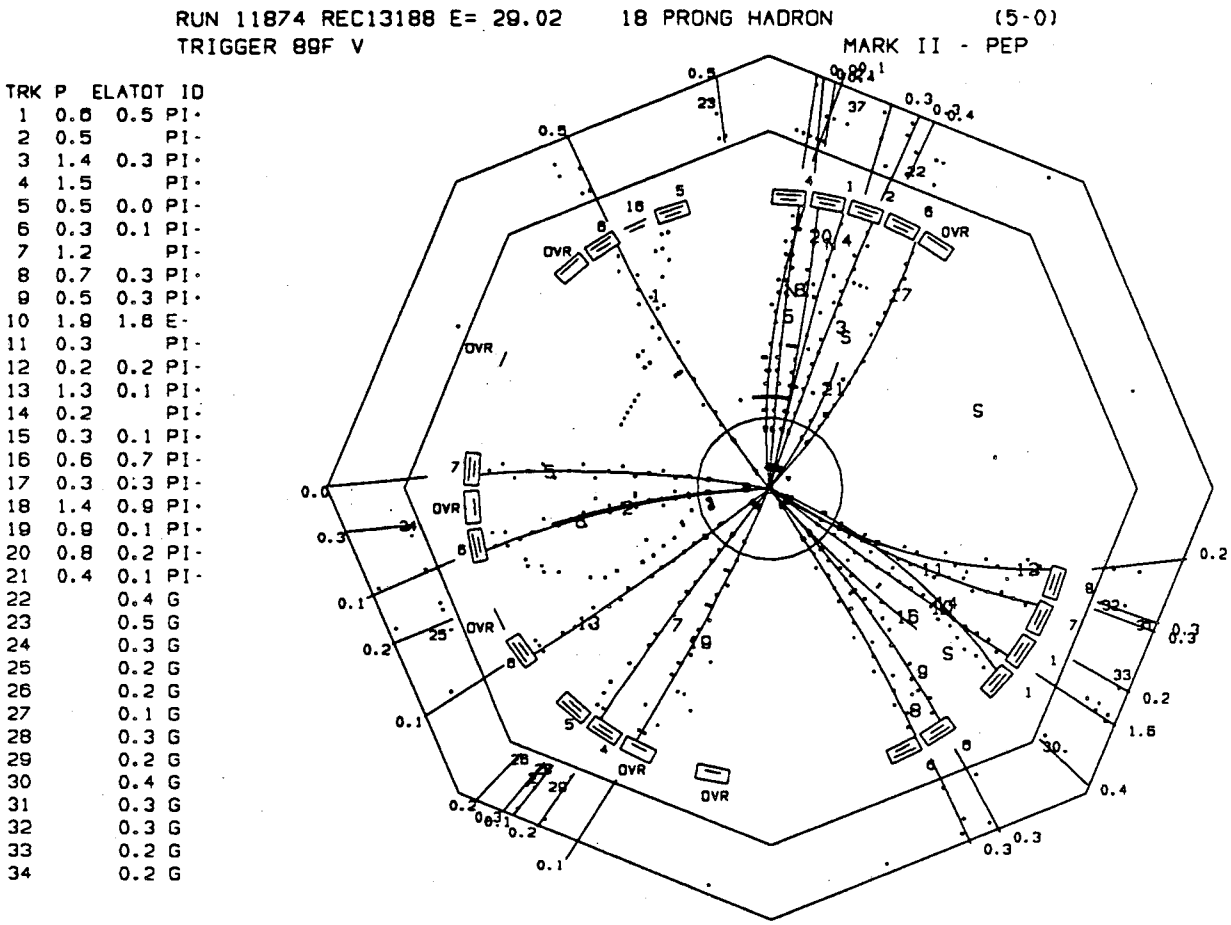

Figure 1.3 *An event showing clear 3-jet structure, observed with the Mark II detector at the PEP e^+e^- storage ring (see Chapter 2) operating at $E_{cm} = 29$ GeV. The event has been projected into the plane perpendicular to the beam axis.*

At this energy, *3-jet* structure is clearly visible (see Fig. 1.3). A good review of the evidence for *3-jet* production is given in Ref. 19.

The order α_s^2 corrections to $\sigma(e^+e^- \rightarrow \textit{hadrons})$ have also been calculated.[20] Just as before, divergences occur in the 4-parton ($e^+e^- \rightarrow q\bar{q}gg, q\bar{q}q\bar{q}$) cross-section when $y_{ij} \rightarrow 0$ for any two of the partons, but when all diagrams[21] are included the total hadronic cross-section is finite. This calculation is extremely difficult, both because of the numerous diagrams and because the results depend on the scheme used to renormalize the quark-gluon coupling constant. In the modified minimal

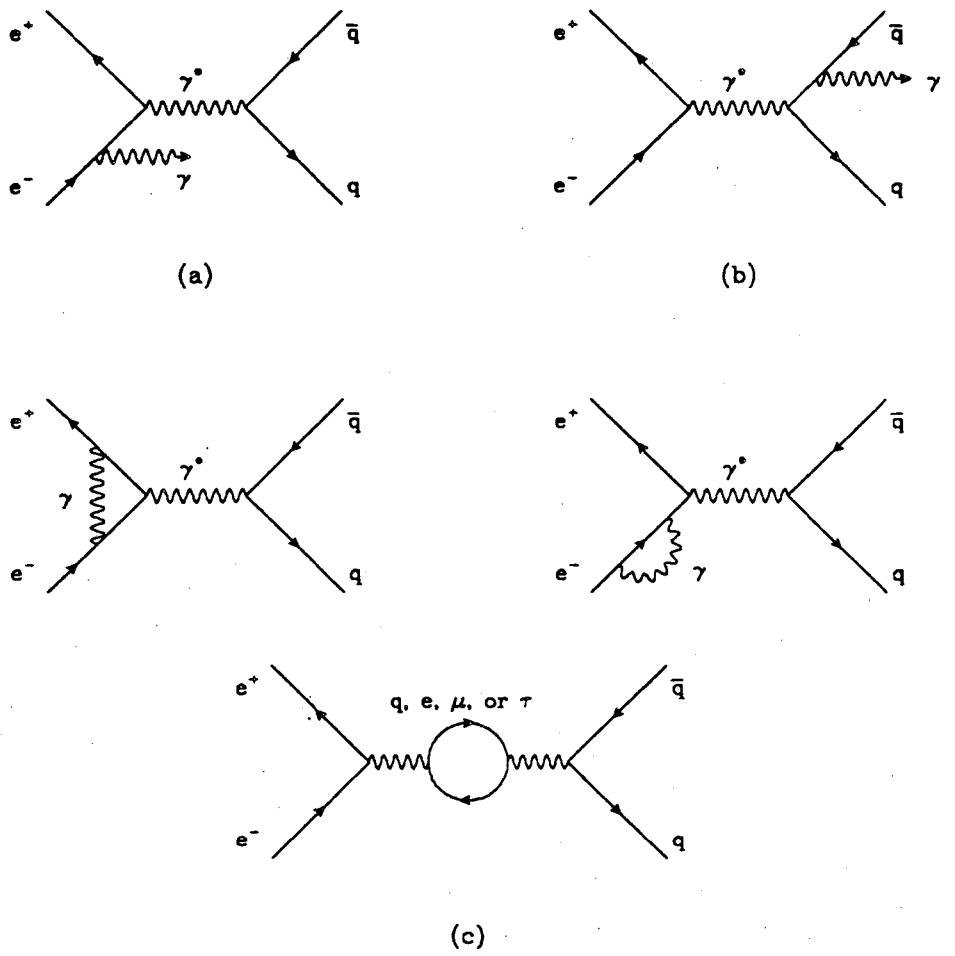

Figure 1.4 *Diagrams for the lowest-order radiative corrections to the process $e^+e^- \rightarrow q\bar{q}$: (a) initial state radiation, (b) final state radiation and (c) initial-state virtual corrections.*

subtraction ($\overline{\text{MS}}$) scheme,

$$\sigma_2 = \sigma_0 \left[1 + \left(\frac{\alpha_s}{\pi} \right) + C_2 \left(\frac{\alpha_s}{\pi} \right)^2 \right] \tag{1.11}$$

where $C_2 = 1.98 - 0.115\, N_f$ and N_f is the number of quark flavors that can be produced at the E_{cm} of interest. At 29 GeV, $\sigma_2 = 1.054\, \sigma_0$. Just as for *3-jet* events, an observable *4-jet* cross-section can be defined by requiring all parton pairs to satisfy $y_{ij} > y_{min}$. If y_{min} is defined as in (1.9), $\sigma^{4\text{-}jet}$ is only a small fraction ($< 5\%$) of the total hadronic cross-section at $E_{cm} = 29$ GeV.

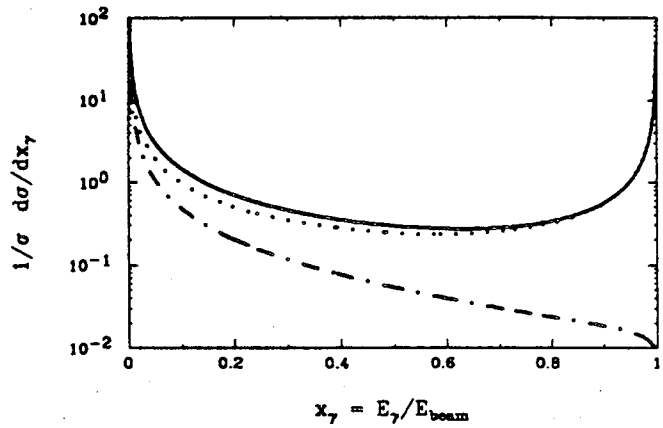

Figure 1.5 *Energy spectrum for photons from initial-state (dotted line) and final-state (dash-dotted line) radiation in hadronic events. The solid line shows the total radiative cross-section. The plot was generated using formulae given in Ref. 22 and is from Ref. 23.*

1.1.3 Radiative Corrections to the Hadronic Cross-Section

The radiative, or higher-order QED, corrections to reaction (1.1) are also important. The equivalent to gluon emission (Fig. 1.2(a)) is photon bremsstrahlung: $e^+e^- \rightarrow q\bar{q}\gamma$. The Feynman diagrams for this process and the other lowest-order radiative corrections are shown in Fig. 1.4.

One difference between photon and gluon bremsstrahlung is that photons can be radiated by either the initial-state particles or the final-state partons. The total, final-state and initial-state radiative cross-sections are shown in Fig. 1.5 as a function of the energy of the radiated photon. The spectrum for final-state photons shows the characteristic $1/E_\gamma$ behavior of bremsstrahlung radiation, but the initial-state cross-section is flat over a large energy range and rises as $E_\gamma \rightarrow E_{beam}$, where $E_{beam} = \frac{1}{2}E_{cm}$. This behavior is the result of the decrease in center-of-mass energy of the annihilating e^+ and e^- after one of them radiates a photon. Since the hadronic cross-section is proportional to $1/s$, the interaction probability rises as E_γ increases, effectively countering the falling photon spectrum. Because of its flat spectrum, initial-state radiation accounts for essentially all of the correction to the total hadronic cross-section.

The cross-section for the process $e^+e^- \rightarrow \gamma + hadrons$ diverges when $E_\gamma \rightarrow 0$, and when $E_\gamma \rightarrow E_{beam}$ uncertainties in the hadronic cross-section arise. Events

of the latter type are not of interest anyway since they are unlikely to produce multi-jet events. Regardless, just as in QCD perturbation theory,

$$\sigma_{tot} = \sigma(e^+e^- \to hadrons) + \sigma(e^+e^- \to \gamma + hadrons)$$

is finite. The formula for σ_{tot} is complicated;[22] but at $E_{cm} = 29$ GeV

$$\sigma_{tot} = 1.34\,\sigma_{had} \tag{1.12}$$

where σ_{had} is the total hadronic cross-section before radiative corrections. Only initial-state diagrams are included in (1.12). Final-state corrections to σ_{had} are[24] less than 0.2%.

If a resolvable radiative hadronic event is one with

$$k_{min} < E_\gamma < k_{max} \equiv (E_{beam} - k_{min})$$

a finite cross-section for radiative events can be calculated

$$\sigma^{rad} = \int_{k_{min}}^{k_{max}} \frac{d\sigma}{dE_\gamma} dE_\gamma$$

$$\sigma^{no\text{-}rad} = \sigma_{tot} - \sigma^{rad}\,.$$

For $k_{min} = 0.01\,E_{beam}$ and $E_{cm} = 29$ GeV, $\sigma^{rad}/\sigma_{tot} = 0.455$.

1.1.4 Total Hadronic Cross-Section

Combining (1.3), (1.4), (1.11) and (1.12), the total hadronic cross-section is

$$\sigma_{tot} = 1.34 \left[1 + \left(\frac{\alpha_s}{\pi}\right) + C_2 \left(\frac{\alpha_s}{\pi}\right)^2\right] \frac{4\pi\alpha^2}{s} \sum_{i=1}^{N} e_{q_i}^2 \tag{1.13}$$

$$= 0.538 \text{ nb} \qquad (\text{at } E_{cm} = 29 \text{ GeV})\,.$$

This calculation includes all of the corrections to the parton model cross-section which are known to be significant at $E_{cm} = 29$ GeV.

1.2 The Effects of Hard Gluon Emission

The goal of this analysis is to study the effects of hard gluon emission on hadron production in e^+e^- annihilation events. These effects allow us to infer the properties of gluons and to test the theory of strong interactions, QCD.

1.2.1 Differences in Gluon and Quark Jets

Quantum Chromodynamics predicts that hard gluon bremsstrahlung will have both local and global effects on hadron production in e^+e^- annihilation events. Locally, the gluon should fragment differently than the quarks in the event, leading to a jet which has a higher multiplicity, a softer momentum distribution and a larger opening angle than quark jets.[3,4] These differences are due to the larger "color charge" of the gluon. The ratio of the gluon and quark color charges is 9/4. Because of this increased charge, the gluon is more likely to radiate the soft gluons which produce hadrons. In the asymptotic limit of QCD ($Q^2 = (E_{jet})^2 \rightarrow \infty$),

$$\frac{\langle n_g \rangle}{\langle n_q \rangle} = \frac{\langle \theta_g \rangle}{\langle \theta_q \rangle} = \frac{9}{4}$$

where $\langle n_g \rangle$ and $\langle n_q \rangle$ are the average multiplicities of gluon and quark jets and $\langle \theta_g \rangle$ and $\langle \theta_q \rangle$ are the average opening angles of these jets. The momentum spectrum of particles from gluon jets will be softer because of this difference in multiplicity. Jet energies currently available in e^+e^- collisions ($E_{jet} < 20$ GeV), however, are too low to approach the asymptotic limit. Although no quantitative QCD predictions exist, the multiplicity and opening angle ratios of these low energy gluon and quark jets are expected to be less than the asymptotic values given above.[25]

We investigate the differences in gluon and quark jets by comparing jets from radiative *2-jet* events with jets from *3-jet* events. The presence of a radiative photon in $q\bar{q}\gamma$ events decreases the energy of the two quark jets and leads to hadronic final states that have a similar topology to $q\bar{q}g$ events. Therefore, radiative *2-jet* events provide us with a source of known quark jets which can be compared with equal

energy gluon and quark jets from *3-jet* events. It is important to compare equal energy jets because jet properties such as momentum distributions do not scale with the energy of the jet.[26] Systematic uncertainties due to event selection and jet finding should be similar for jets from these two types of events because they have analogous topologies.

1.2.2 Hadron Production in Three-Jet Events

Because the gluon carries color charge, it distorts the color field of the primary quark and anti-quark in *3-jet* events, and affects hadron production in the event globally. Recent QCD calculations[8] predict a depletion of particles in the angular region between the q and $\bar{q}$ jets relative to the number of particles in the region between the q and g jets or the region between the $\bar{q}$ and g jets. Because the gluon in *3-jet* events is replaced by a photon in radiative *2-jet* events, comparisons of the number of particles between the q and $\bar{q}$ jets in these two types of events allow us to observe this depletion directly.

Predictions of a depletion of particles between the q and $\bar{q}$ in *3-jet* events are based on QCD calculations of the soft gluon production probability between the partons in a given $q\bar{q}\gamma$ or $q\bar{q}g$ configuration.[8] Consider the case of the emission of a soft gluon g_2 in a $q\bar{q}\gamma$ event. The angular distribution of g_2 is given by

$$\begin{aligned} W_{q\bar{q}\gamma}(\hat{\mathbf{n}}_2) &= 2\,C_F \frac{(1-\hat{\mathbf{n}}_q\cdot\hat{\mathbf{n}}_{\bar{q}})}{(1-\hat{\mathbf{n}}_q\cdot\hat{\mathbf{n}}_2)\,(1-\hat{\mathbf{n}}_{\bar{q}}\cdot\hat{\mathbf{n}}_2)} \\ &= 2\,C_F\,A_{q\bar{q}}(\hat{\mathbf{n}}_2) \end{aligned} \tag{1.14}$$

where $C_F = (N_c^2-1)/2\,N_c = 4/3$ ($N_c = 3$ is the number of colors in QCD) and $\hat{\mathbf{n}}_i$ is the normalized direction vector of parton i. Close to the partons, this calculation is not valid. This distribution is the gluon emission probability for a *2-jet* event, boosted from the $q\bar{q}$ center-of-mass system into the lab frame. The source of hadrons in a $q\bar{q}\gamma$ event is therefore in motion in the lab frame.

For the more complex $q\bar{q}g$ system, the angular distribution of g_2 is given by

$$W_{q\bar{q}g}(\hat{\mathbf{n}}_2) = N_c\, A_{qg}(\hat{\mathbf{n}}_2) + N_c\, A_{\bar{q}g}(\hat{\mathbf{n}}_2) + (2\,C_F - N_c)\, A_{q\bar{q}}(\hat{\mathbf{n}}_2) \qquad (1.15)$$

Comparing (1.14) and (1.15), we see that the emission probability in $q\bar{q}g$ events is effectively the sum of the probability from three "color dipoles" formed by the qg, $\bar{q}g$ and $q\bar{q}$. The radiation pattern from each of these dipoles is identical in form to the pattern from the $q\bar{q}$ system in $q\bar{q}\gamma$ events. Each "dipole" is therefore in motion in the lab frame. Due to destructive interference, the intensity of the radiation from the $q\bar{q}$ dipole is reduced by a factor

$$\frac{(N_c - 2C_F)}{N_c} = \frac{1}{N_c^2} = \frac{1}{9}$$

relative to the radiation from the qg and $\bar{q}g$ dipoles.

Because the sources of particles in these events are in motion in the lab frame and because radiation from the $q\bar{q}$ dipole is significantly diminished, fewer soft gluons are produced in the angular region between the q and $\bar{q}$ in $q\bar{q}g$ events, and this region is depopulated. Consider a hadron with energy E^* and momentum $\vec{\mathbf{p}}^*$, produced by a soft gluon in the rest frame of a dipole. In the lab frame, where the dipole has velocity βc, the component of the hadron's momentum in the boost direction $\hat{\mathbf{n}}_\beta$ is

$$\vec{\mathbf{p}} \cdot \hat{\mathbf{n}}_\beta = \gamma \vec{\mathbf{p}}^* \cdot \hat{\mathbf{n}}_\beta + \gamma\beta E^* \qquad (1.16)$$

while the components orthogonal to the boost direction remain unchanged. Hadrons therefore gain momentum in the boost direction. Since there is little radiation from the $q\bar{q}$ dipole, hadrons tend to be boosted out of the region between the q and $\bar{q}$, and this region is depleted relative to the angular regions between the q and g and between the $\bar{q}$ and g. This depletion can be observed directly by comparing particle production between the q and $\bar{q}$ jets in $q\bar{q}g$ events with particle production in this region in $q\bar{q}\gamma$ events, where destructive interference does not diminish the radiation from the $q\bar{q}$ dipole.

Finally, from (1.16) we see that the fractional increase in momentum of a particle in the boost direction is proportional to $E^*/(\hat{\mathbf{n}}_\beta \cdot \vec{\mathbf{p}}^*)$. As a result, the depletion predicted above will be larger for particles with large transverse masses

$$m_\perp = [(m)^2 + (p_\perp^{(out)})^2]^{1/2} \tag{1.17}$$

where $p_\perp^{(out)}$ is the momentum component of a particle out of the event plane.

Chapter 2. The Mark II Detector at PEP

From 1980 to 1984, the Mark II detector collected electron-positron interactions produced by the Positron Electron Project (PEP), a large e^+e^- storage ring 2.2 km in circumference located at the Stanford Linear Accelerator Center. Equal energy beams of electrons and positrons, each concentrated in three highly localized bunches, circulate in opposite directions in the ring. An electron and positron bunch meet every 2.4 μsec at six interaction regions, producing e^+e^- annihilation events at a peak rate of roughly one per minute. During the four years the Mark II ran at PEP, the ring operated at a center-of-mass energy (E_{cm}) of 29 GeV.

2.1 The Mark II Detector

The Mark II detector at PEP was a general purpose magnetic detector with approximate cylindrical symmetry about the axis defined by the circulating beams. Two views of the detector are given in Fig. 2.1. In the central region of solid angle, the Mark II had (at progressively larger radii)

- inner and central drift chambers immersed in a solenoidal magnetic field to provide charged particle tracking,
- a layer of scintillators located just inside the magnet coil to measure the time-of-flight (TOF) of charged hadrons and aid in their identification,
- a lead and liquid argon electromagnetic calorimeter to detect electrons and photons, and
- four layers of proportional counter tubes and thick steel plates which were used to tag muons.

The design of these components naturally suggests the cylindrical coordinate system used throughout this dissertation: r and φ are the radius and azimuthal angle measured in the plane orthogonal to the beam, or z, axis. Another commonly used coordinate is the polar angle θ, measured with respect to the z axis.

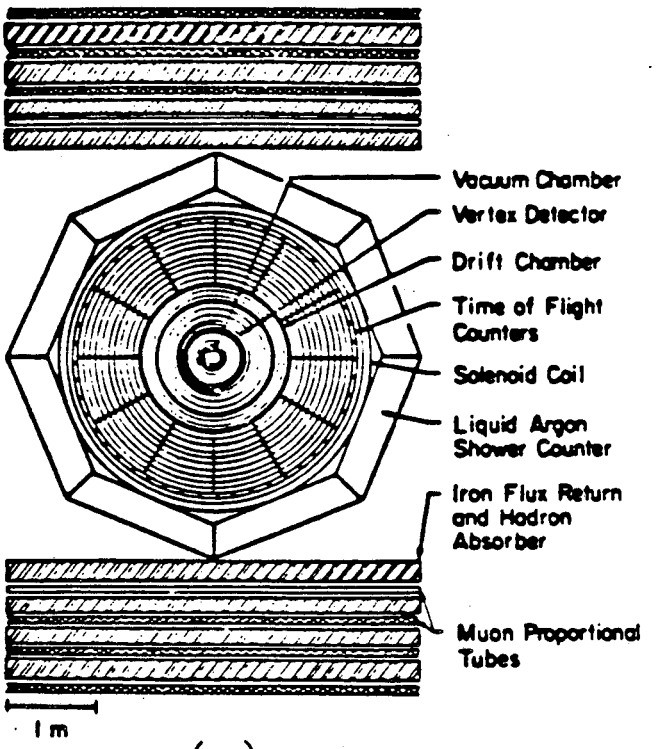

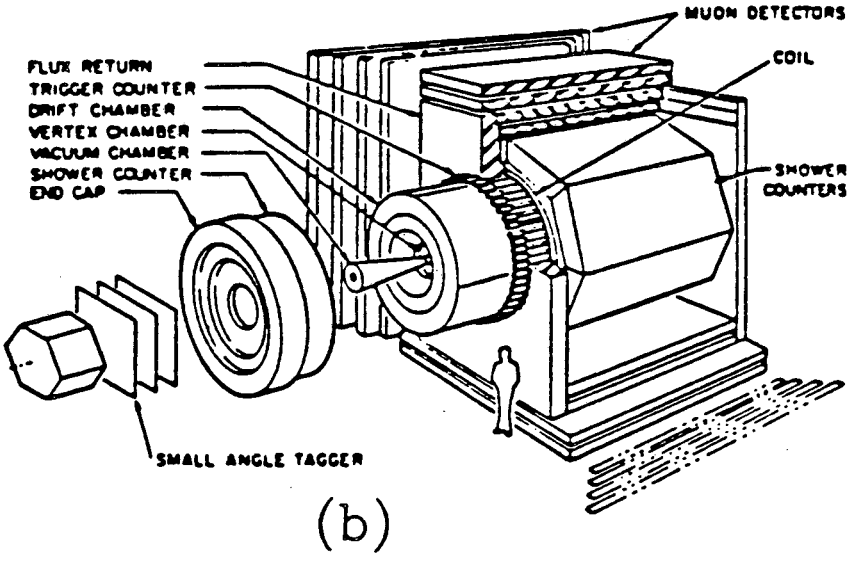

Figure 2.1 *Two views of the Mark II detector at PEP: (a) a slice of the detector taken perpendicular to the beam axis, and (b) an isometric view.*

To observe electromagnetic showers in the forward regions, the detector had lead and proportional chamber endcap calorimeters. In the very forward regions a small angle tagging (SAT) system, consisting of planes of drift chambers followed by lead and scintillator shower counters, was used to identify electrons produced at small polar angles. From the rate of Bhabha electron pairs detected with the SAT system, the storage ring luminosity was determined with an accuracy of 5%. Events were read out and written to magnetic tape by a Vax 11/780 computer, which was also responsible for monitoring the detector on-line.

The main detector components used in this analysis, the charged particle tracking system and the liquid argon calorimeter, are described briefly below. Previous publications[27] contain detailed descriptions of the Mark II detector.

2.1.1 Charged Particle Tracking System

A charged track completely traversing both of the cylindrical drift chambers of the Mark II deposited ionization in 23 concentric layers of drift cells. The inner chamber was a high resolution vertex detector designed to accurately measure the position of secondary vertices resulting from particle decays. Four thin bands of axial sense wires at a radius of 11.5 cm and three more at 31 cm shared a common gas volume filled with a mixture of 50% argon and 50% ethane at 1 atmosphere. The sense wires were spaced about 1 cm apart in φ and the spatial resolution of the chamber was typically 110 μm per layer.

The central drift chamber consisted of 16 layers of drift cells, equally spaced between the first and last layers at radii of 41 and 145 cm. Again the chamber had a common gas volume of 50% argon and 50% ethane at atmospheric pressure. The 6 innermost layers had a sense wire spacing of 1.8 cm, the 10 outer layers a spacing of 3.6 cm. The average spatial resolution of each cell was about 220 μm. Successive layers had stereo angles of 0°, +3°, and −3° with respect to the beam axis in order to provide z information. The combined inner and central chambers afforded charged particle tracking over 80% of 4π in the central region.

Momenta of charged tracks were determined from their curvature in the mag-

netic field of the solenoid, which consisted of two coils of water-cooled aluminum conductor and originally produced a 4.64 kG field. Very early in the run at PEP a short developed between the two layers of the coil; thereafter only the outer coil was powered. Roughly 90% of the data were collected while the Mark II was in this 2.3 kG configuration. The momentum resolution of the drift chambers in the half-field configuration was

$$\left(\frac{\delta p_\perp}{p_\perp}\right)^2 = (0.025)^2 + (0.01\, p_\perp)^2$$

where $p_\perp$ is the particle momentum, in GeV/c, in the r-φ plane. The first term is due to multiple scattering, and the second term is the measurement error. The momentum resolution in the full-field configuration was very similar because the inner drift chamber was (coincidentally) installed at approximately the same time that the magnet short developed. The inner chamber improved the measurement error by providing track information at small r, effectively countering the loss of resolution due to the decrease in magnetic field.

2.1.2 Liquid Argon Calorimeter

The central calorimeter was comprised of eight self-contained modules arranged in an octagonal array around the magnet coil. Each module consisted of 37 antimony strengthened lead planes, 2 mm thick, separated by 3 mm liquid argon gaps. Solid ground planes alternated with 3.5 kV readout planes which were segmented into strips. The strips ran parallel to the beam in 9 of the readout planes, and were perpendicular to this direction in 6 others. These strips were 3.8 cm wide. In the remaining 3 planes, used for ambiguity resolution, 5.4 cm wide strips ran at a 45° angle to the beam direction. About 20% of the shower energy was deposited in the liquid argon. At the front of each module was a "massless" gap designed to identify showers which had begun in the 1.25 radiation length magnet coil. This gap consisted of three aluminum planes separated by 8 mm of liquid argon; the middle plane served as a readout plane.

The calorimeter was 14.5 radiation lengths thick, and covered 64% of 4π in the central region. Its energy resolution was

$$\frac{\delta E}{E} = \frac{0.14}{\sqrt{E}} \qquad (E \text{ in GeV})$$

and its spatial resolution as determined by Bhabha electrons was 7 mm.

2.2 EVENT TRIGGER

Because the beam crossing rate of 400 kHz was much larger than the e^+e^- event rate of about 0.01 Hz, a two stage trigger was used to decide whether or not to record an event on magnetic tape. The primary trigger logic, composed of separate charged track, neutral energy and Bhabha triggers, was fast enough to reject events between beam crossings. The charged track trigger required hits in several drift chamber layers and in at least one time-of-flight scintillator. An event was accepted by the neutral energy trigger if it had energy deposits (greater than some minimum) in 2 of the 8 liquid argon calorimeter modules or if the total energy in the liquid argon and endcap calorimeters was larger than a threshold. Finally, if there were hits in the SAT system consistent with a small angle Bhabha, the Bhabha trigger was satisfied.

If the primary trigger was satisfied, a programmable secondary trigger used fast electronics to look for track patterns in the drift chambers, associated time-of-flight hits and energy deposits in the calorimeters. Typically, this trigger was satisfied if

- two or more tracks were found and at least one of these tracks had an associated TOF hit,
- 1 GeV of energy was deposited in at least 2 liquid argon modules,
- there was more than 4 GeV of total energy in the liquid argon and endcap calorimeters, or
- the Bhabha primary trigger fired.

The secondary trigger took 30 μsec to make a decision, resulting in a dead time of 3% per kHz of primary trigger rate. Normally, the primary rate was approximately

1 kHz, and the secondary rate was around 3 Hz. The trigger was greater than 99% efficient for hadronic events which passed reasonable quality cuts (see Chapter 3).

2.3 Event Reconstruction

Events were reconstructed off-line with an IBM 3081 computer. First, a pattern recognition program searched the raw data output of the vertex and central drift chambers for charged track candidates, which were fit to a helix. An event vertex was found by constraining all charged tracks to originate from a common point in space. Tracks missing this origin by a large distance or contributing greatly to the χ^2 of the vertex fit were not included. Data in the other detector systems were then associated with the tracks. Finally, the calorimeters were searched for photons, and the fully reconstructed events were written on summary tapes.

Chapter 3. Event Selection

In order to make accurate comparisons of *3-jet* ($q\bar{q}g$) and radiative *2-jet* ($q\bar{q}\gamma$) events, systematic differences between the two samples must be minimized. The selection process is therefore as identical as possible for the two event types. Briefly, this process begins with the culling of hadronic events from the full data set. These events are searched for radiative photon (γ_{rad}) candidates. Radiative *2-jet* events are selected from events with a γ_{rad}, and *3-jet* events from those without such a photon. In this chapter, this procedure and the resulting data samples are described in detail.

3.1 Hadronic Event Selection

The full data sample taken by the Mark II detector at $E_{cm} = 29$ GeV has a total integrated luminosity of 227 pb^{-1}. According to (1.13), this corresponds to 122,000 produced hadronic events. Alternative sources of events with particle multiplicities which can mimic those of hadronic events are:

- *pair production of τ leptons*: If one or both τ's decay hadronically, events with more than 4 charged tracks that carry a large fraction of E_{cm} can result. However, 97% of these $\tau^+\tau^-$ events have a charged multiplicity of 4 or less.
- *2-photon processes*: $e^+e^- \rightarrow e^+e^- + hadrons$ (see Fig. 3.1). Although this higher-order QED process is an important contribution to the total cross-section at 29 GeV, the distribution of the center-of-mass energy W of the hadrons peaks at zero and falls off rapidly.
- *"beam-gas" events*: Interactions of the beam with residual gas in the beam pipe may lead to high multiplicity events, but their event vertices are evenly distributed along the beam direction and they have a W spectrum similar to that for 2-photon events.

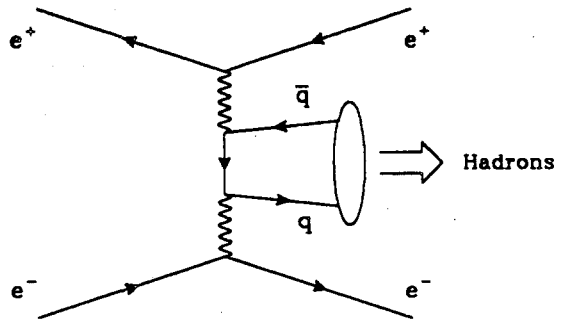

Figure 3.1 *Feynman diagram for 2-photon production of hadrons.*

Our hadron selection cuts are designed to reduce contributions from these processes.

Charged tracks used in this analysis are required to have momenta greater than 100 MeV/c in the plane transverse to the beam axis and to have $|\cos\theta| \leq 0.8$ with respect to this axis. A track's closest approach to the beam interaction point must be within 10 cm in z and 5 cm in r. For tracks with momenta less than 1 GeV/c, the cut on r is loosened to $r \cdot p \leq 5$ cm GeV/c to account for multiple scattering errors. Photons included in this analysis must deposit at least 250 MeV in the liquid argon calorimeter and be farther than 7 cm (at the radius of the calorimeter) from the closest charged track.

In order to obtain a clean sample of hadronic events, we require an event to have at least 5 charged tracks and $E_{vis} \geq 0.25\, E_{cm}$, where E_{vis} is the linear sum of the energies of charged tracks and photons. The event's reconstructed primary vertex must be within 5 cm of the beam spot center in the r-φ plane, and within 10 cm in z. These cuts reduce the background from the sources described above to less than 4% of the total events.[26] Finally, to insure that the event is adequately contained in the detector, its thrust axis[28] must satisfy $|\cos\theta| \leq 0.7$. The thrust axis is defined as the unit vector $\hat{\mathbf{n}}$ which maximizes

$$T = \frac{\sum_i |\vec{\mathbf{p}}_i \cdot \hat{\mathbf{n}}|}{\sum_i |\vec{\mathbf{p}}_i|}$$

where the sums are over all the charged and neutral tracks defined above. After applying these cuts, we obtain 72,757 events.

3.2 Monte Carlo Event Samples

To aid the study of efficiencies, backgrounds and systematic errors in hadronic events we have generated several Monte Carlo event samples. In general, these samples are produced by using a standard event-generation package to create e^+e^- hadronic events. These packages use finite-order QCD perturbation theory or QCD parton shower theory to obtain a primordial state of quarks and gluons (see for example Fig. 1.2(a)). These partons are then "fragmented" into final-state particles. Short descriptions of the two generators used in this dissertation are given in Appendix A. The generated events are then run through a detailed simulation of the Mark II detector, which produces raw detector responses to the particles along their flight paths through the detector. Energy loss, multiple scattering, photon conversion, and nuclear interactions in the detector material are taken into account in the simulation. The resulting raw "data" are then analyzed with the Mark II off-line event reconstruction code, resulting in Monte Carlo event samples of similar quality to the actual data.

Primarily, we use a large Monte Carlo event sample generated with the Lund string fragmentation model[29] An equivalently sized sample of Ali independent fragmentation model[30] events is also utilized. The number of events in these samples is approximately equal to the expected number of hadronic events in our data sample. Simulations of first-order initial-state radiative processes[31] are included in both of these models. Events with final-state radiation do not contribute significantly to the total cross-section, and such events are not produced by the standard event generators. However, since we are studying radiative events, we have also generated a sample of events with a version of the Lund model modified to simulate both initial and final-state radiative processes.[23,31] This sample has one-third fewer events than our standard Lund model sample, and it is only used in specific situations where the effects of final-state radiation are significant.

In both the Lund and Ali generators, the cutoff parameters used when calculating $\sigma^{3\text{-}jet}$ and $\sigma^{4\text{-}jet}$ (see (1.8)) determine the relative number of 2, 3 and 4-parton states generated. It has been shown[32] that small y_{min} cuts ($y_{min} \approx 0.015$)

Table 3.1 *Monte Carlo event samples.*

Name	*Comment*
Lund	standard Lund model
Ali	standard Ali model
Modified Lund	Lund model with final-state radiation
Radiative Lund	Lund events, all with initial-state radiation
Radiative Ali	Ali events, all with initial-state radiation
No-Boost Ali	like Radiative Ali, but events fragmented in the lab frame

are necessary to fully reproduce hadronic data. For example, even though 3-parton events with low values of y_{min} will not produce observable *3-jet* events, such events provide necessary higher-order corrections to *2-jet* events. In our sample of Lund model events, generated with $y_{min} = 0.02$, 24% are $q\bar{q}$ events, 68% are $q\bar{q}g$ events and 8% are $q\bar{q}gg$ or $q\bar{q}q\bar{q}$ events. Because many of these $q\bar{q}g$ events are not observable *3-jet* events, we use a larger cut, $y_{min} = 0.05$, in our definition of 2, 3 and 4-parton events. For instance, a 3-parton event is a $q\bar{q}g$ event with $y_{min} > 0.05$, or a $q\bar{q}gg/q\bar{q}q\bar{q}$ event which fails this cut. With this definition, 62% of the events in our Lund sample are 2-parton events, 37% are 3-parton events and 1% are 4-parton events.

Names and characterizations of all the Monte Carlo event samples we use are listed in Table 3.1. Event samples listed in the table and not discussed above will be described later. In order to make comparisons with the data straightforward, we have normalized all of our Monte Carlo samples to have the same effective luminosity as our data. The input parameters used when generating events with the Ali and Lund models are given in Appendix B.

Table 3.2 *The number of particle clusters (m) found by the cluster algorithm in hadronic events without radiative photon candidates. The predictions of the Lund Monte Carlo are also given. Events with $m = 1$ had no distinct clusters.*

m	*Data*	*Lund*
1	1,634	1,764
2	59,372	60,919
3	8,161	7,159
4	158	60
5	1	1
All	69,326	69,903

3.3 THREE-JET EVENTS

3.3.1 Selection

We select $q\bar{q}g$ candidates from hadronic events without radiative photon candidates, which are defined below. The Lund cluster algorithm[33] is used to find clusters (jets) of charged and neutral particles in the events. The cluster algorithm initially treats the m particles in the event as separate "clusters". The two closest clusters are combined, leaving $m-1$ clusters. This step is repeated until the distance between all cluster pairs is greater than d_{min}, or until there is only one cluster. After several iterations, it is possible that a particle in one of the clusters being combined will be farther from the combined cluster than it is from some other cluster in the event. Therefore, after each iteration, all particles are reassigned to the closest cluster. Distance is measured between any two objects (particles and/or clusters) i and j using the metric

$$d_{ij}^2 = \frac{4\, p_i^2\, p_j^2\, \sin^2(\theta_{ij}/2)}{(p_i + p_j)^2}$$

where p_i is the magnitude of the momentum of i and θ_{ij} is the angle between i and j. This metric, for small θ_{ij}, is roughly the transverse momentum squared of i (or j)

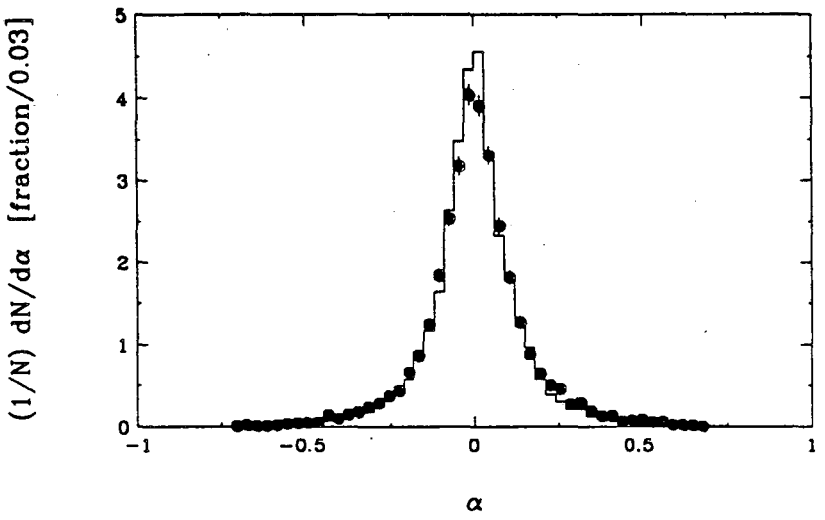

Figure 3.2 *The planarity (α) of candidate 3-jet events in our data (points) and our Lund sample (histogram). The distributions are normalized so that their area is one. For a perfectly measured 3-jet event, $\alpha = 0$.*

with respect to the combination of i and j. A cutoff distance of $d_{min} = 2.5$ GeV/c is used in this analysis.

Table 3.2 shows the distribution of m, the number of clusters found in an event, for all hadronic events without a γ_{rad} candidate. The same result for our sample of Lund Monte Carlo events is also shown. Events with one cluster occur for spherical events with no apparent jet structure. We select events with three clusters as *3-jet* candidates. There is a significant difference in the number of 3-cluster events found in the data and in our Lund Monte Carlo sample. The reason for this will be discussed later.

For these three-cluster events, jet direction vectors or axes are found from the vector sum of the momenta of all members of a cluster. If $\hat{\mathbf{n}}_i$ is the normalized axis of jet i, we require $|\alpha| \leq 0.35$, where $\alpha \equiv \hat{\mathbf{n}}_1 \cdot (\hat{\mathbf{n}}_2 \times \hat{\mathbf{n}}_3)$, to insure that the events are planar. The normalized α distributions for both our data and our sample of Lund events are shown in Fig. 3.2. The Monte Carlo underestimates the width of this distribution, indicating that the jet direction resolution in our Lund sample is slightly optimistic.

We specify an event plane using the eigenvectors of the thrust tensor. These

vectors are found by defining $\hat{\mathbf{e}}_1$ to be the standard thrust axis. A "thrust axis" is then found in the plane perpendicular to $\hat{\mathbf{e}}_1$; this axis is $\hat{\mathbf{e}}_2$. The final eigenvector, $\hat{\mathbf{e}}_3 = \hat{\mathbf{e}}_1 \times \hat{\mathbf{e}}_2$, determines the event plane. Occasionally, the projections of the three jet axes in the event plane occupy only half of the plane, which violates momentum conservation. This occurs when the jet axes of an event are poorly measured, and these events are discarded.

Jet energies are calculated from the angles between the projections of the jet axes in the event plane

$$x_i \equiv \frac{E_i}{E_{beam}} = \frac{2\,\beta_j\,\beta_k\,\sin\phi_i}{\beta_2\,\beta_3\,\sin\phi_1 + \beta_1\,\beta_3\,\sin\phi_2 + \beta_1\,\beta_2\,\sin\phi_3} \tag{3.1}$$

where i, j, and k are cyclic, ϕ_i is the angle between jets j and k, $E_{beam} = \frac{1}{2}\,E_{cm}$, and $\beta_i \equiv v_i/c$ is the velocity of jet i. Jet velocities are calculated using the detected cluster momenta and energies, which are determined using the momenta and energies of the tracks (charged tracks are assumed to be pions) assigned to the clusters. Equation (3.1) can easily be derived from the energy-momentum balance equations

$$\sum_{i=1}^{3} x_i = 2$$

$$\sum_{i=1}^{3} \frac{\vec{P}_i}{E_{beam}} = \sum_{i=1}^{3} \beta_i\,x_i\,\hat{\mathbf{n}}_i = 0\,.$$

The jets are labelled according to their energy, with jet 1 the most energetic and jet 3 the least energetic. It will be shown later that calculating the jet energies using the angles between the jets is much more accurate than the observed cluster energies.

Figure 3.3(a) shows the x_1 distribution for both the data and our Lund model events. Also shown in the plot is the Lund prediction for the 2-parton contribution to the distribution. The Lund model does not completely reproduce the high side of the spectrum. This is probably due to the y_{min} cutoff of the $q\bar{q}g$ cross-section in the

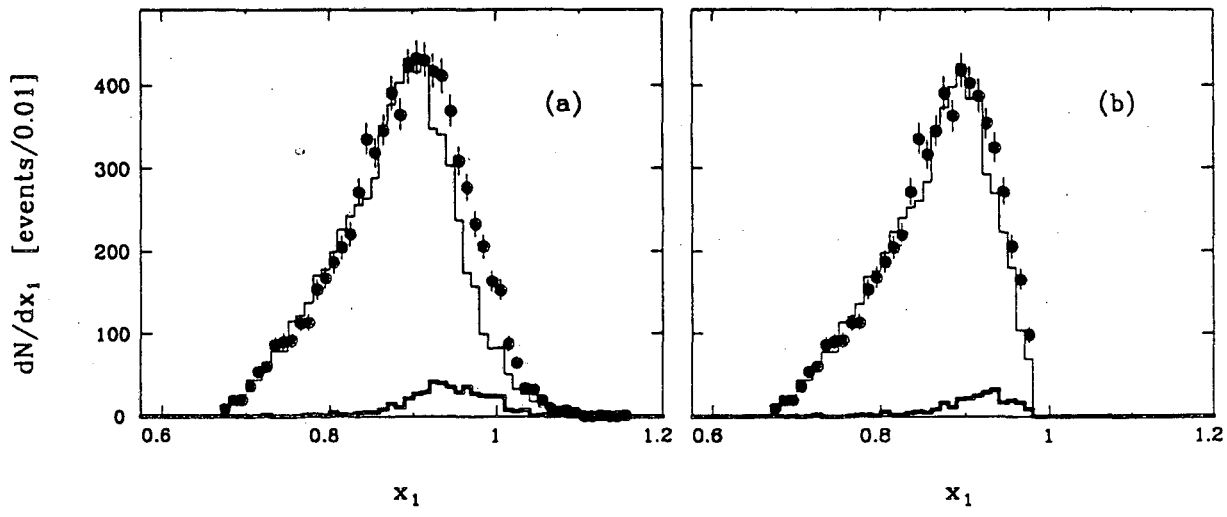

Figure 3.3 *The normalised energy of jet 1 (x_1) for 3-jet candidates (a) before our x_1, ϕ_{min} and E_3 cuts and (b) after these cuts. The lighter histograms in both plots show x_1 for Lund Monte Carlo events, and the darker histograms give the Lund predictions for the 2-parton contributions to these distributions.*

Lund model, which for massless partons is equivalent to a cut on x_1 (increasing y_{min} makes the disagreement in Fig. 3.3(a) significantly worse). Monte Carlo predictions in this region are also very sensitive to the fragmentation parameters used. This failure of the model (which is not specific to the Lund generator) is the reason fewer 3-cluster events are found in our Lund event sample than in our data (see Table 3.2).

To reduce the 2-parton background in our sample of *3-jet* events, we discard events with $x_1 > 0.98$. The smallest angle between any two jets in the event plane (ϕ_{min}) must be greater than 45°to insure that the jets in the event are well separated. Finally, we require $E_3 \geq 3.0$ GeV for reasons discussed below. By eliminating many of the events in our sample with small values of y_{min}, these last two cuts significantly improve the agreement in the x_1 distributions from our data events and from our Lund model events (see Fig. 3.3(b)). After all cuts, 6284 *3-jet* events remain in our data sample. In our Lund Monte Carlo sample, 6049 events are left after all cuts are made, and 4.4% of these are 2-parton events. If all of the discrepancy (*i.e.* the excess of 235 events in our data sample at high x_1) in Fig. 3.3(b) is due to an underestimation of the 2-parton background by the Lund

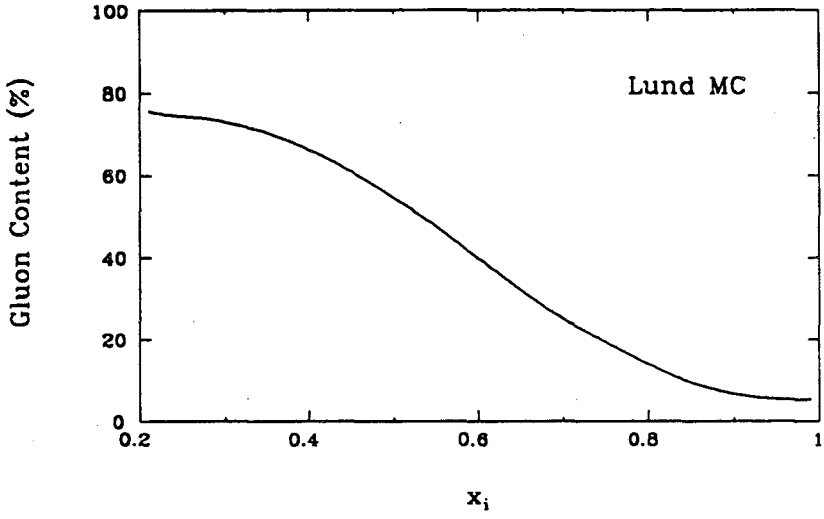

Figure 3.4 *The prediction of the Lund Monte Carlo for the Gluon Content, or percentage of the time that a jet is the gluon jet, versus jet energy. Because we have made a cut on the minimum jet energy in an event, there is no prediction for* $x_i < 0.2$.

Monte Carlo, the 2-parton background in our *3-jet* sample is 8.0%. A typical *3-jet* event is shown in Fig. 1.3.

The Lund prediction for the fraction of the time that a jet is the gluon jet is shown as a function of the jet's energy in Fig. 3.4. Jets 1, 2 and 3 are produced by the gluon 11%, 25% and 59% of the time, respectively. These probabilities do not add to 100% because of the 2-parton background.

3.3.2 Jet Energy and Direction Resolution

We have investigated our ability to reconstruct jets using the 3-parton events in our Lund sample which are selected as *3-jet* events by the procedure described above. There are 5717 such events. The study consists of comparing events as observed in a perfect detector with the same events as seen in the Mark II. The perfect detector finds all particles in an event, determines their momenta and energies without error and assigns tracks to jets exactly.[34] The cosine of the angle between the directions of a jet as found with a perfect detector and with the Mark II ($\cos\delta$) is plotted in Fig. 3.5. This quantity is plotted separately for jets 1, 2 and 3. Since high energy jets are thinner than low energy jets, measurements of their direction

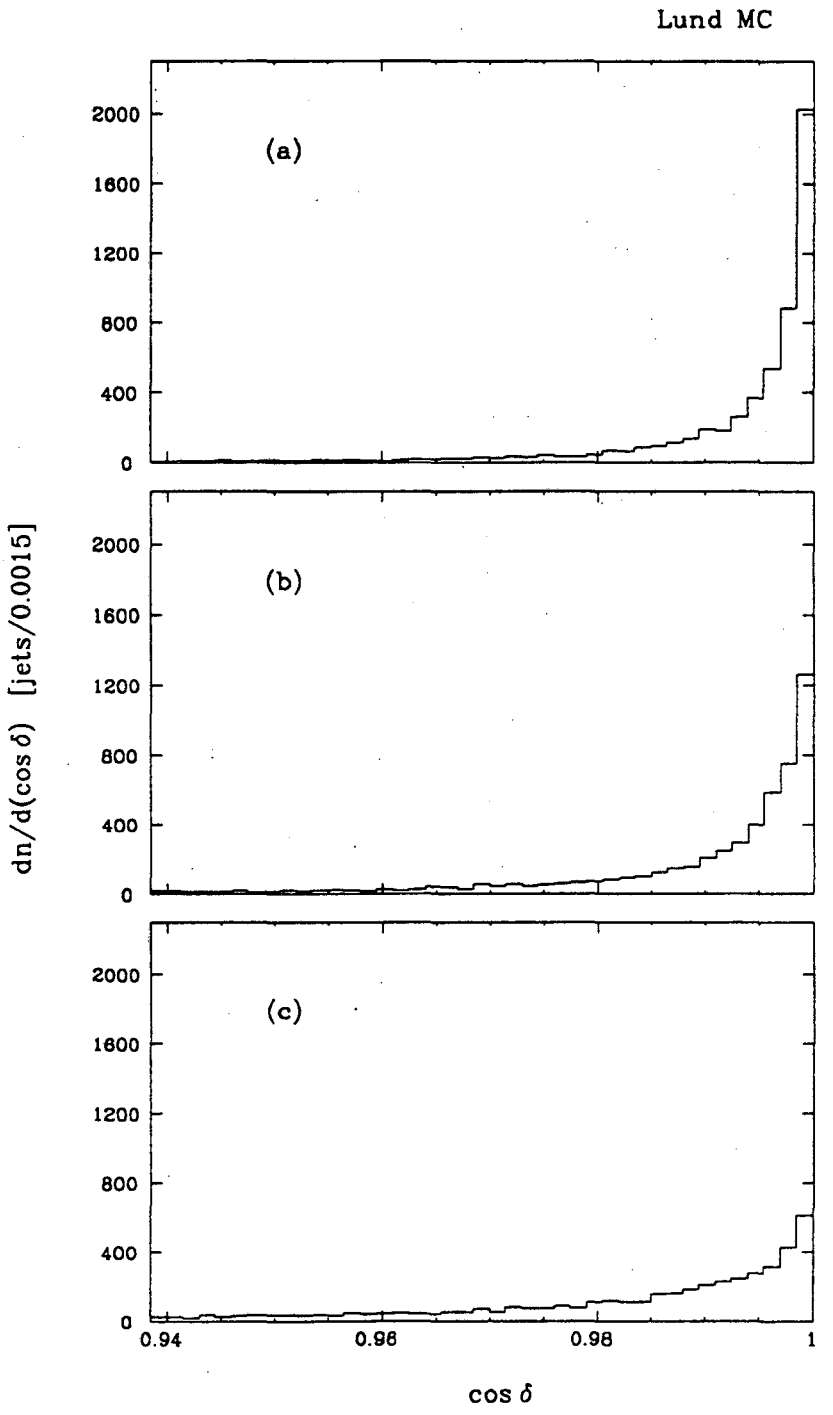

Figure 3.5 *The cosine of the angle (δ) between a jet's direction found using the Mark II and using an ideal detector. Our Lund Monte Carlo events were used to make the study. The plots show the results for (a) jet 1, (b) jet 2 and (c) jet 3.*

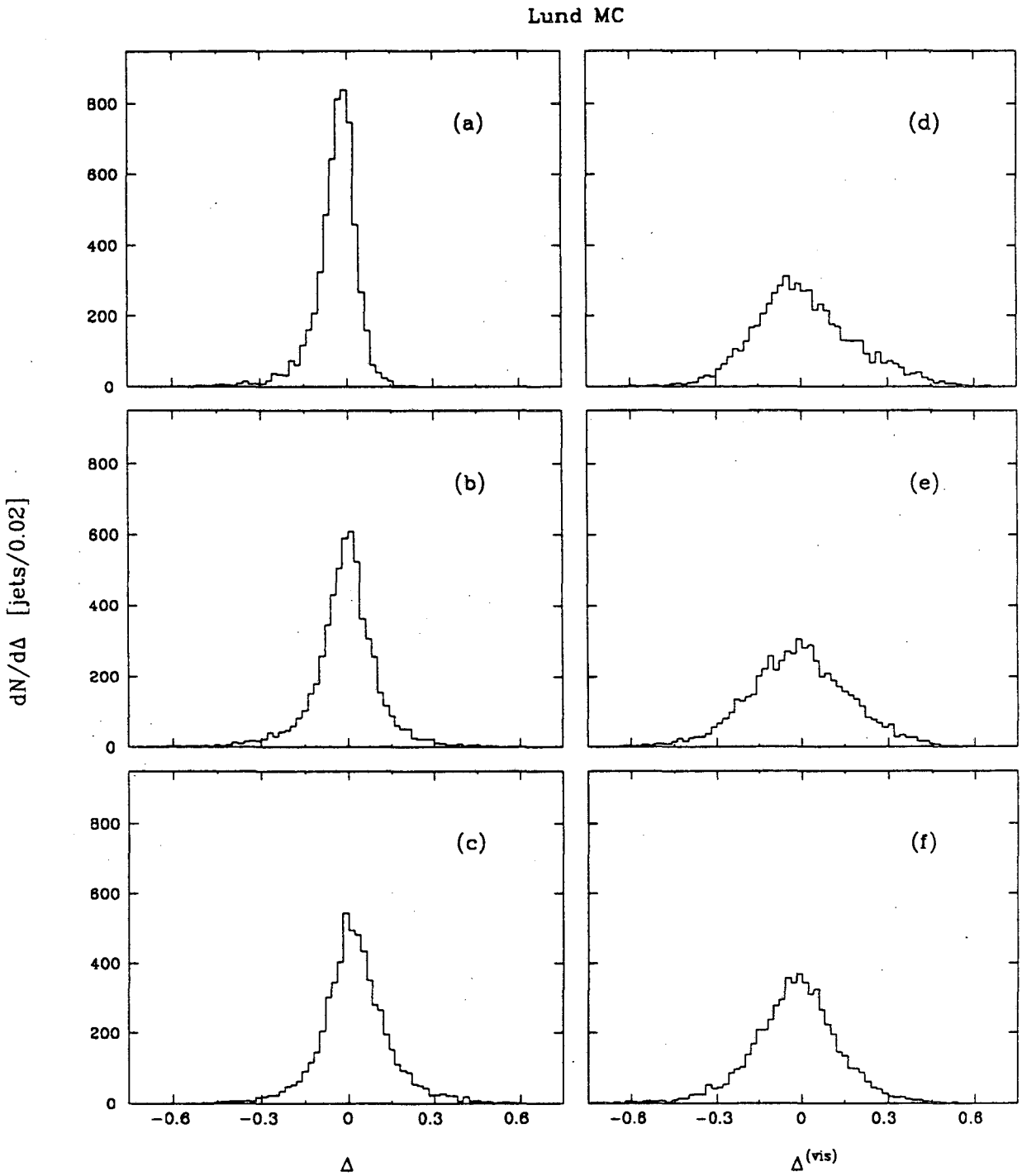

Figure 3.6 *The jet energy resolution in Lund Monte Carlo events for (a) jet 1, (b) jet 2 and (c) jet 3. If the energy of a jet is determined using its visible energy, the resolution is much worse. This is shown in (d)–(f) for (d) jet 1, (e) jet 2 and (f) jet 3. There are 5717 jets in each plot.*

vectors are less influenced by detector effects such as missing or poorly measured tracks, and are therefore more accurate. Our jet energy resolution shows similar tendencies since we determine the energy of jets using their direction vectors. This can be seen in Figs. 3.6(a)–3.6(c), where we plot

$$\Delta_i \equiv \frac{E_i^{(p)} - E_i}{E_{beam}} = x_i^{(p)} - x_i$$

($E_i^{(p)}$ is the energy of jet i as measured in the perfect detector). The average of $\cos\delta$ over all jets is 0.983, which corresponds to $\delta = 10.5°$. Similarly, $\sigma(\Delta_i) = 0.108$, equivalent to an energy resolution of 1.57 GeV.

The visible energy of a jet ($E_i^{(vis)}$), calculated from the sum of the energies of its assigned tracks, is less accurate than the energy calculated using (3.1). This indicates that jet directions are better preserved after detector effects than visible jet energies. This is true even if the visible energies are scaled so that their sum is E_{cm}:

$$x_i^{(vis)} = 2E_i^{(vis)} \Big/ \sum_{j=1}^{3} E_j^{(vis)} \ .$$

In Figs. 3.6(d)–3.6(f), we plot

$$\Delta_i^{(vis)} = x_i^{(p)} - x_i^{(vis)} \ .$$

The resolution in this case, $\sigma(\Delta_i^{(vis)}) = 0.170$ (2.47 GeV), is significantly larger than $\sigma(\Delta_i)$ above.

3.4 Radiative Two-Jet Events

3.4.1 Identification of Radiative Photons

The problem of separating radiative photons from other, non-direct sources of photons (mainly π^0 decay) is simplified by our interest in photons with energies on the order of resolvable hadronic jets: $E_\gamma \geq 3.0$ GeV. Radiative photons with this much energy will be well separated from any hadronic jets in the event, whereas

Table 3.3 *The number of clusters (m) found in hadronic events with a radiative photon candidate. For an $m = 3$ event, the cluster algorithm found two clusters, and the photon is the third cluster. The predictions of our Lund and Modified Lund Monte Carlo samples are also given.*

m	*Data*	*Lund*	*Modified Lund*
2	637	589	630
3	2552	2096	2243
4	239	172	184
All	3431	2857	3057

photons from meson decay will be members of the jets. In addition, the energy spectrum for non-direct photons peaks near zero and falls off rapidly. For this analysis, if a photon has $E_\gamma \geq 2.5$ GeV and there are no moderately energetic ($p \geq$ 500 MeV/c) charged tracks within a 30° cone around the photon, it is considered a radiative candidate. If more than one photon in a given event passes these cuts, we choose the one with the highest energy. At this point our goal is to find true radiative photons with a high efficiency, so our selection criteria are deliberately lax. As a result, a majority of these radiative candidates are from non-direct sources. Subsequent cuts will reduce this background considerably. A candidate photon (γ_{rad}) is found in 3431 of our hadronic events.

3.4.2 Radiative Two-Jet Event Selection (Method I)

Radiative *2-jet* events are selected from hadronic events with radiative photon candidates. All tracks except γ_{rad} are used in the cluster search, 2-cluster events are selected, and the photon is included as a third "jet". The distribution of the number of clusters m found in each event is given in Table 3.3. The photon "cluster" has been included in the definition of m. The difference in the number of events found in the data and our Lund sample is partially due to the fact that the Lund model does not include final-state radiative processes. The number of events found in our Modified Lund sample, which includes both initial and final-state radiation,

Table 3.4 *The number of events in our $q\bar{q}\gamma$ sample after various cuts are made. The cuts are made in the order listed in the table. The abbreviation "p-bal" stands for our momentum balance cut (described in the text).*

Cuts	*Data*	*Modified Lund*
None	2552	2243
α, p-bal	1543	1437
x_1, ϕ_{min}, E_3	594	635
All	544	585

is in better agreement with the data.

These radiative *2-jet* events are then treated like the *3-jet* events discussed earlier in that the jet energies $E_1 > E_2 > E_3$ are calculated using the angles between the projections of the jets in the event plane, and the same cuts on α, momentum balance, x_1, ϕ_{min} and E_3 are applied (the "momentum balance" cut just removes events in which all three jet axes lie in only half of the event plane). Table 3.4 gives the number of events in our $q\bar{q}\gamma$ sample after various cuts are made. Because we previously required radiative photons to deposit at least 2.5 GeV in the calorimeter, the cut on E_3 assures consistent kinematics in the $q\bar{q}g$ and $q\bar{q}\gamma$ samples. Note that for these events, $\beta = 1$ is used for the photon jet in (3.1). To insure that the photon energy measured in the liquid argon calorimeter ($E_\gamma^{(LA)}$) is consistent with its energy calculated from (3.1) ($E_\gamma^{(angles)}$), we require $|\Delta_\gamma| \leq 0.3$, where

$$\Delta_\gamma \equiv \frac{E_\gamma^{(LA)} - E_\gamma^{(angles)}}{E_{beam}} = x_\gamma^{(LA)} - x_\gamma^{(angles)} .$$

In Fig. 3.7(b), the Δ_γ distribution is plotted for events after all cuts except the one on Δ_γ. There are 544 radiative *2-jet* events that pass all cuts. In these events, jet 1, 2 or 3 is the photon jet 18%, 24% or 58% of the time, respectively. The γ_{rad} energy spectrum is given in Fig. 3.8 for our selected $q\bar{q}\gamma$ events, one of which is shown in Fig. 3.9. As discussed in Chapter 1 (see Fig. 1.5), the spectrum is relatively flat.

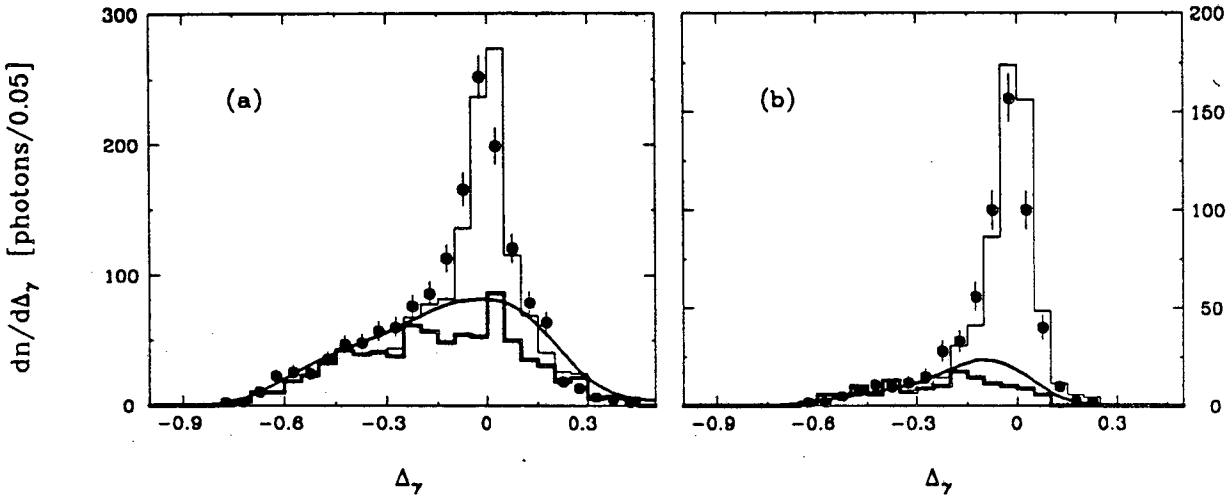

Figure 3.7 *The difference between x_γ measured in the liquid argon calorimeter and x_γ calculated using (3.1), (a) before and (b) after the x_1, ϕ_{min} and E_3 cuts. The points in both plots are from our $q\bar{q}\gamma$ data, and the light histograms give the distributions for our Modified Lund model, which simulates both initial and final-state radiation. This model's predictions for the non-radiative photon contamination are shown as dark histograms in these plots. The curves in both plots are from our fake photon sample (see text).*

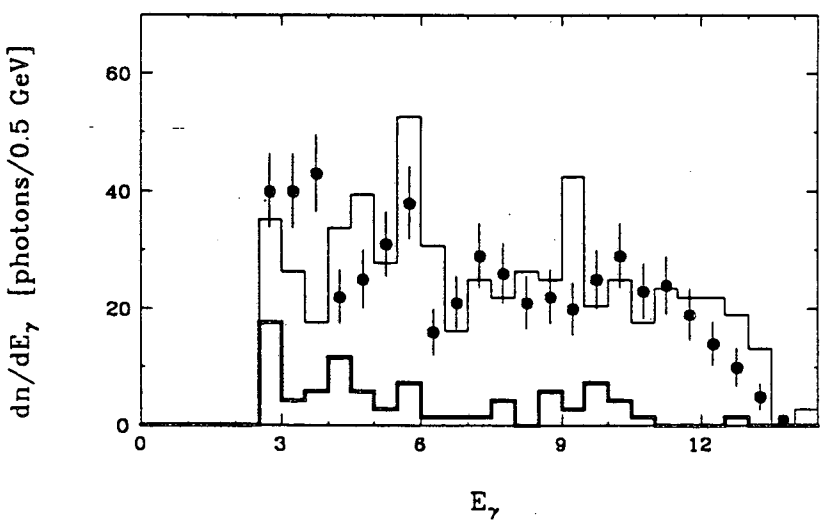

Figure 3.8 *The γ_{rad} energy spectrum for method I $q\bar{q}\gamma$ events in our data (open circles), and modified Lund model (light histogram) samples. The dark histogram shows the spectrum for non-radiative photons as predicted by our modified Lund Model.*

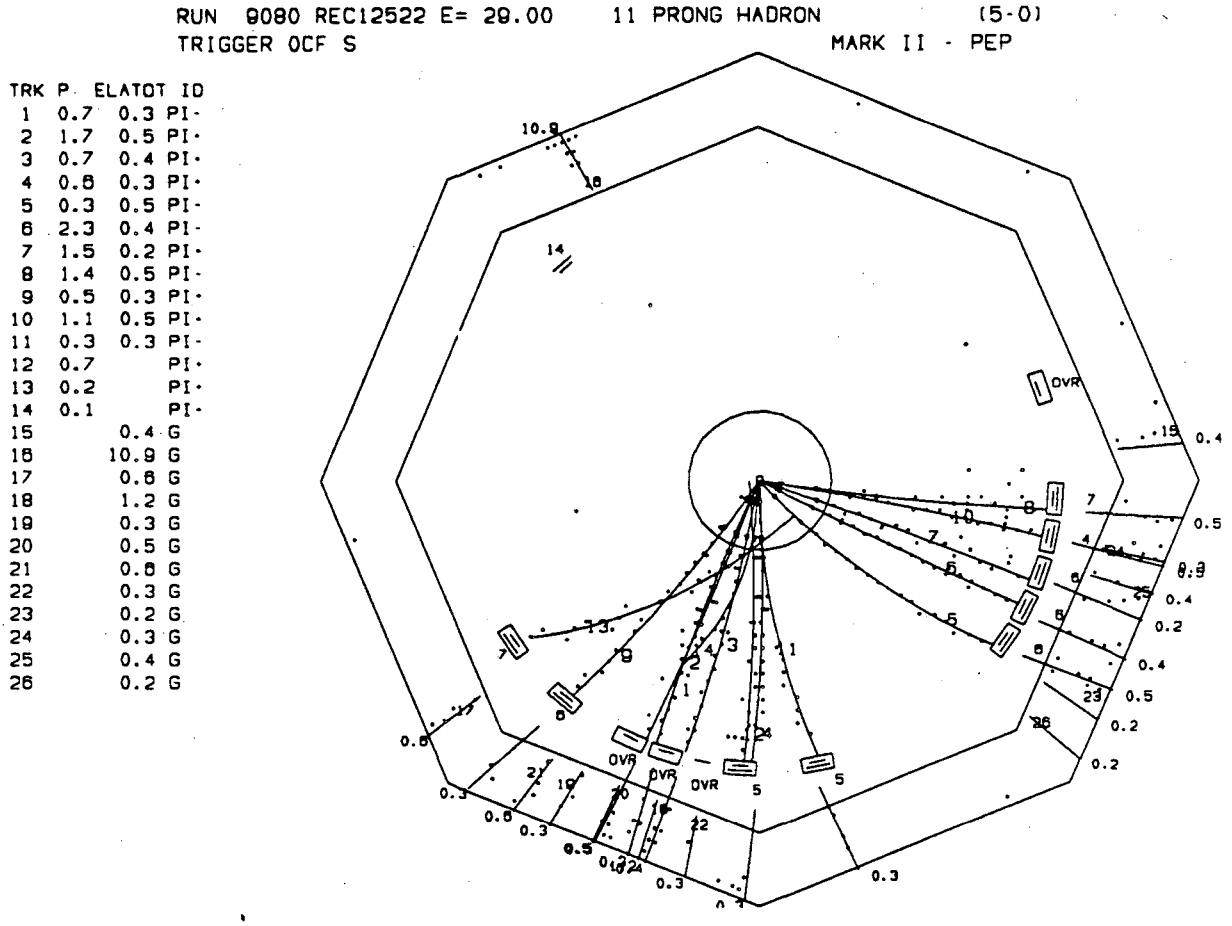

Figure 3.9 *A radiative two-jet event, shown projected in the plane perpendicular to the beam axis. The only activity in the top half of the detector is a 10.9 GeV photon in the upper left module of the liquid argon calorimeter (the large outer octagon).*

The expected rise at $E_\gamma \simeq E_{beam}$ is not seen because our hadron selection and cluster finding procedures have a low efficiency for these events. The γ_{rad} spectra for $q\bar{q}\gamma$ events selected from our Modified Lund Monte Carlo (light histogram) and for non-radiative background events as predicted by this model (dark histogram) are included in the figure.

3.4.3 The Non-Radiative Background

Non-direct photons such as those from π^0 decay are produced relatively abundantly compared to energetic radiative photons, and it is important to understand

their contribution to our $q\bar{q}\gamma$ sample. Our cuts on ϕ_{min}, x_1 and E_3 should eliminate much of this background because hadronic sources generally produce photons which are close to the jets in the event. In addition, the Δ_γ distribution for these events should be much broader than for true radiative events. This is because the visible energy of jets, which in this case is simply $E_\gamma^{(LA)}$, is not a very good measure of jet energies as was shown earlier in this chapter. In a true radiative photon "jet", however, there are no associated missing or poorly measured tracks. Therefore, $E_\gamma^{(LA)}$ is an excellent measure of the jet energy and the width of the Δ_γ distribution should be significantly smaller. In Fig. 3.7(a), we show the Δ_γ distribution for $q\bar{q}\gamma$ candidates before the x_1, $\phi_{min}$and E_3 cuts. The gaussian shaped peak of Fig. 3.7(b) is still visible in Fig. 3.7(a), but there is also a broad background distribution evident. The number of events in Figs. 3.7(a) and 3.7(b) are given in Table 3.4.

The Δ_γ distributions predicted by our Modified Lund Monte Carlo are given by the light histograms in Fig. 3.7. Although not shown, the statistical errors on the distributions in these histograms are roughly equal in size to those shown for the data. Taking this into account, the Monte Carlo and data distributions in the figure are in agreement. According to this Modified Lund model, 15% of our final sample of $q\bar{q}\gamma$ events are non-radiative events. The Δ_γ distributions for these non-radiative photons are given by the dark histograms in Fig. 3.7.

As a cross-check on the shape of the background distribution in Fig. 3.7, we have studied a sample of fake photons which should behave much like our non-radiative background. To obtain this sample, we select radiative *2-jet* events using exactly the same procedure as described above except that we choose γ_{rad} (using the same cuts as before) from the *charged* tracks in the event. These charged tracks are mainly π^+ and π^- mesons, just as most of our non-radiative photons come from π^0 mesons. The smooth curves drawn in Figs. 3.7(a) and 3.7(b) show the Δ_γ distributions for these fake photons. Our fake events, which have been normalized to approximately fit the long background tail between $-0.9 < \Delta_\gamma < -0.3$ in Fig. 3.7(a), cannot account for the gaussian bump at $\Delta_\gamma = 0$. The effect of our x_1, $\phi_{min}$and E_3 cuts

on this fake event sample can be seen in Fig. 3.7(b).

Although most of our non-radiative background comes from π^0 decay, and most of our fake events from charged π's, the shape of the Δ_γ distributions for these two samples will not be identical. For $\Delta_\gamma < -0.3$, the curves from our fake sample agree with our Monte Carlo predictions of the Δ_γ distributions for our background events (dark histograms). Near $\Delta_\gamma = 0$, however, these distributions differ. This difference occurs because non-radiative photons share the π^0 energy with a second photon, so that Δ_γ is less likely to be zero for these photons than for our fake photons. Our fake sample, then, overestimates the background in the signal region.

3.4.4 Radiative Two-Jet Event Selection (Method II)

Greatly simplified, the action of the cluster algorithm is to assign tracks to the closest cluster (keeping in mind that distance is not measured in a spatial coordinate system). In *3-jet* events, this sometimes results in "track-assignment confusion": a track produced at a large angle to its parent parton will be assigned to another, closer jet in the event. For $q\bar{q}\gamma$ events selected via the procedure described above, however, no other track in the event is ever assigned to the photon jet, even if it is closer to the photon than it is to its assigned jet. For much of this analysis, the cluster algorithm is used only to find jet directions and energies. Track-assignment confusion (or the lack of it) does not greatly affect the found jet directions and energies because the few tracks produced at large angles to the jet axis have low momenta. However, in portions of our analysis where the actual assignment of tracks to jets is important, differences in track-assignment confusion could possibly lead to systematic differences in the two event samples.

When track assignments are important, we will use a second method of $q\bar{q}\gamma$ event selection. Method II events are again selected from the 3431 hadronic events with γ_{rad} candidates, and the difference in the two selection methods lies completely in the clustering procedure. Instead of selecting 2-cluster events found using all tracks except γ_{rad}, in method II we include γ_{rad} in the cluster search and select 3-cluster events. The cluster containing γ_{rad} is the photon jet, and 75% of the visible

Table 3.5 *Distribution of the number of tracks assigned to the photon jets in our final sample of method II $q\bar{q}\gamma$ events.*

tracks	*Data*	*Modified Lund*
1	55.0%	61.2%
2	25.5	24.6
3	12.6	10.6
4	5.0	2.4
5	1.4	1.2
≥ 6	0.5	0.0

energy in this jet must be contributed by γ_{rad} or the event is rejected. The rest of the selection procedure is identical to method I. In the selected events, a track which is closer to the photon than to the other clusters in the event will be assigned by the cluster algorithm to the photon jet, and the track-assignment confusion of large angle tracks will be partially present. However, $q\bar{q}g$ and $q\bar{q}\gamma$ events can never have identical track-assignment systematics because the photon does not fragment, hence no tracks from the photon feed into the other jets in the event.

After all cuts, there are 420 method II radiative 2-jet events, and jet 1, 2 or 3 is the photon jet 24%, 27% or 49% of the time, respectively. According to our Modified Lund model, 7% of these events are background. The distribution of the number of tracks (including γ_{rad}) assigned to the photon jets in our final sample of method II $q\bar{q}\gamma$ events is given in Table 3.5. The average number of tracks in the photon jet is 1.75. Methods I and II select almost the same events, as 94% of the events in our method II final sample are also in our method I final sample. Method I selects more events because it has a higher efficiency for finding events with low energy radiative photons. Such events tend to be found as 2-cluster events by method II.

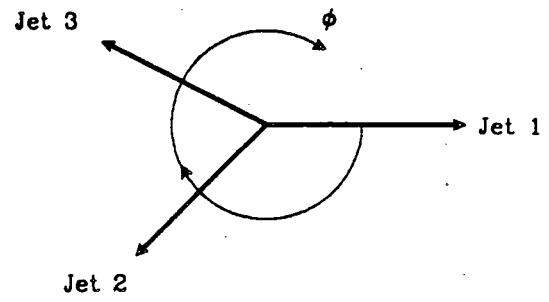

Figure 3.10 *Definition of the event-plane angle ϕ.*

3.5 Comparison of the Data Sets

One of the important features of these $q\bar{q}\gamma$ and $q\bar{q}g$ events is that, because they have similar kinematics and topologies, they should have nearly identical systematic errors. How similar these events are can be seen by comparing the energy and event-plane angle distributions of their jets. For each of the jets in the selected $q\bar{q}\gamma$ and $q\bar{q}g$ events, an event-plane angle ϕ is measured relative to the projection of jet 1, with the direction of increasing ϕ toward jet 2 (see Fig. 3.10). By definition, then, jet 1 has $\phi = 0$ and jet 2 has a smaller value of ϕ than jet 3. Table 3.6 gives the average jet energies and angles for the two types of events. The errors quoted in the table are statistical only. Method I is used to select the $q\bar{q}\gamma$ events, but the results presented are identical within statistical errors to those obtained if method II is used. In Fig. 3.11, ϕ is plotted for jets 2 and 3 from $q\bar{q}g$ and $q\bar{q}\gamma$ events. The energy distributions for jets 1, 2 and 3 are given in Fig. 3.12. There is good agreement between the two data sets, and the Lund model (whose predictions are also shown in the table and the figures) reproduces the data well.

Table 3.6 *The average jet energies and event-plane angles for jets from $q\bar{q}g$ and method I $q\bar{q}\gamma$ events. For jet 1, $\phi \equiv 0$. The errors quoted are statistical only.*

	Data		Lund MC	
Quantity	$q\bar{q}g$	$q\bar{q}\gamma$	$q\bar{q}g$	$q\bar{q}\gamma$
$\langle x_1 \rangle$	0.8671 ± 0.0008	0.8714 ± 0.0030	0.8626 ± 0.0009	0.8654 ± 0.0032
$\langle x_2 \rangle$	0.7089 ± 0.0011	0.7139 ± 0.0036	0.7097 ± 0.0011	0.7099 ± 0.0038
$\langle x_3 \rangle$	0.4240 ± 0.0013	0.4147 ± 0.0049	0.4277 ± 0.0014	0.4247 ± 0.0051
$\langle \phi_2 \rangle$	152.01 ± 0.13	151.82 ± 0.49	151.67 ± 0.14	151.03 ± 0.53
$\langle \phi_3 \rangle$	234.66 ± 0.19	233.47 ± 0.74	235.02 ± 0.19	235.62 ± 0.87

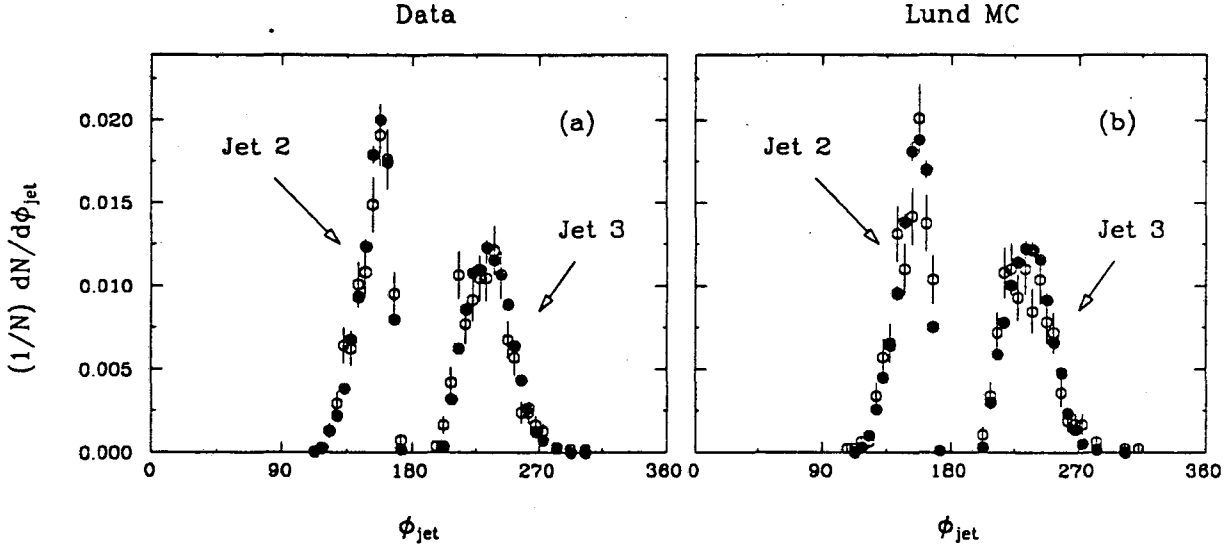

Figure 3.11 *The event plane angle (ϕ) for jet 2 and jet 3 in $q\bar{q}g$ (solid points) and method I $q\bar{q}\gamma$ (open circles) events. For jet 1, $\phi \equiv 0$. Plot (a) shows the results for our data, plot (b) for our Lund sample. The distributions for each sample are normalised by the number of events in that sample, and the bin size in the plots is 5°. In some bins the data points overlap and the open circles are hidden.*

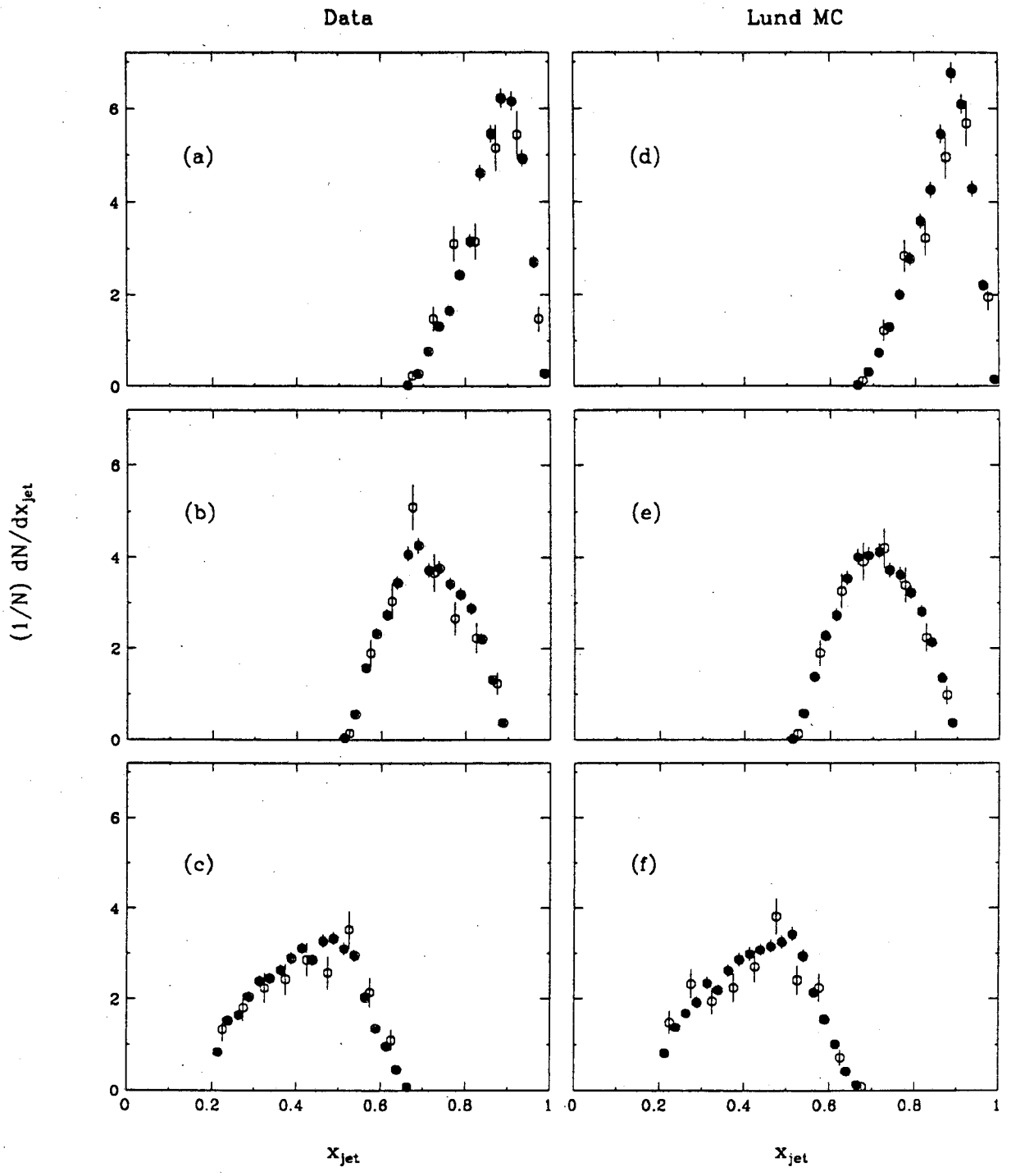

Figure 3.12 *The jet energy distributions for (a) jet 1, (b) jet 2 and (c) jet 3 from $q\bar{q}g$ (solid points) and method I $q\bar{q}\gamma$ (open circles) events. Plots (d)–(f) show the results for (d) jet 1, (e) jet 2 and (f) jet 3 in our Lund sample. The distributions for each sample are normalized by the number of events in that sample, and the bin size in the plots is 0.05.*

Chapter 4. Particle Densities in the Event Plane

Because the gluon carries color charge, it distorts the color field of the primary quark and anti-quark, and affects hadron production in the event globally. In particular, QCD predicts that destructive interference of soft gluon emission from the q, $\bar{q}$ and g will lead to a depletion of particles in the angular region between the quark and anti-quark jets relative to the region between the quark and gluon jets or the region between the anti-quark and gluon jets.[8] Because the gluon in *3-jet* events is replaced by a photon in radiative *2-jet* events, comparisons of these two types of events allow us to observe the effects of hard gluon emission on particle production in hadronic events.

4.1 Method and Results

If a depletion of particles is present in the angular region between the q and $\bar{q}$ jets in $q\bar{q}g$ events, it should occur principally between jets 1 and 2 since jet 3 is the gluon jet 59% of the time. To compare particle production in this region, the $q\bar{q}\gamma$ events of interest are those in which the photon is jet 3. There are 315 such events in our method I sample of radiative *2-jet* events. In Fig. 4.1(a), we plot

$$\rho(\phi) \equiv \frac{1}{N_{events}} \frac{dn_{tracks}}{d\phi}$$

the charged track density in $q\bar{q}g$ and $q\bar{q}\gamma$ events as a function of the event-plane angle ϕ. In the angular region between $\phi = 0°$ and $\phi = 150°$, which separates the q and $\bar{q}$ in all of the $q\bar{q}\gamma$ events and in 59% of the $q\bar{q}g$ events, the figures show a relative depletion in the $q\bar{q}g$ data. If this depletion is due to QCD coherence, it should be enhanced for particles with large transverse masses (see (1.17)). Figure 4.1(b) shows the charged track density for tracks with $|p_\perp^{(out)}| \geq 300$ MeV/c, and the depletion does appear to be enhanced. We have also included in the plots the predictions of the Lund string fragmentation and the Ali independent fragmentation models

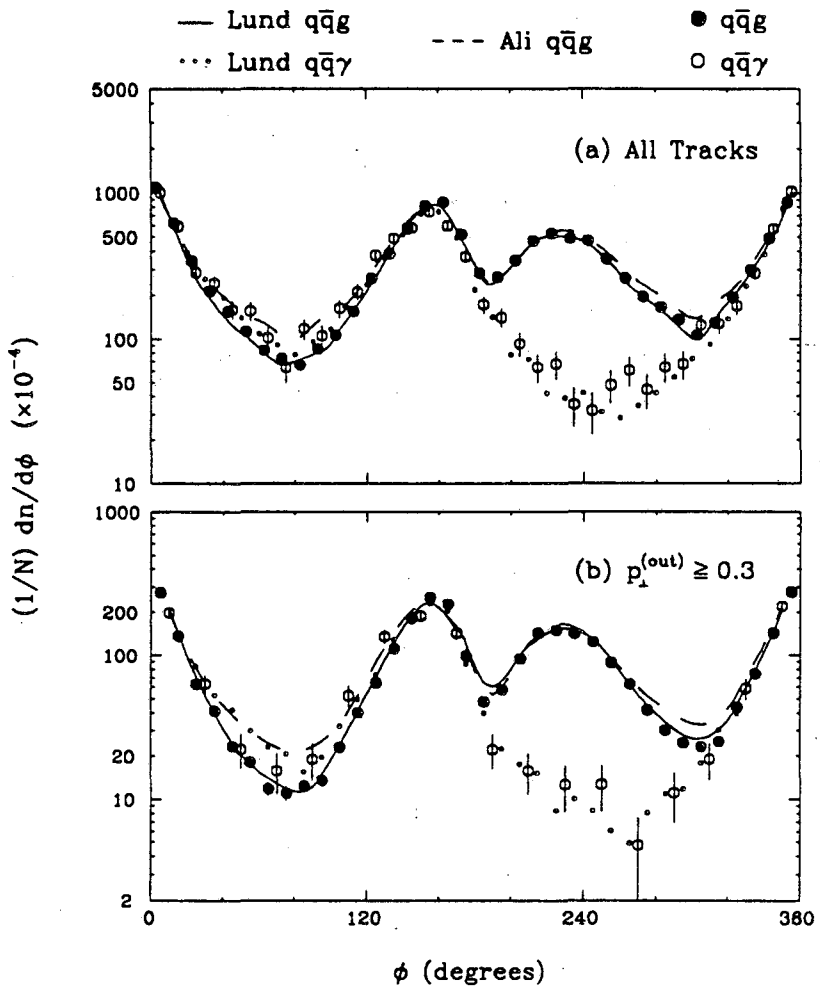

Figure 4.1 *The charged track density as a function of the event-plane angle ϕ. The angular region between $\phi = 0°$ and $\phi = 150°$ separates the q and $\bar{q}$ in all of the $q\bar{q}\gamma$ events and in 59% of the $q\bar{q}g$ events. The density is shown for (a) all charged tracks and (b) charged tracks with $|p_\perp^{(out)}| \geq 300$ MeV/c.*

for $\rho(\phi)$ from $q\bar{q}g$ events. It has already been shown[9,10] that the Lund model reproduces this depletion for *3-jet* events, while independent fragmentation models such as the Ali model do not (see Appendix A). Both models behave as expected in Fig. 4.1.

Because our Lund $q\bar{q}\gamma$ events have limited statistics, we have produced a large sample of Lund hadronic events that are required to have initial-state radiation. The radiative photons in these events must have $|\cos\theta_\gamma| \leq 0.7$, so that they will

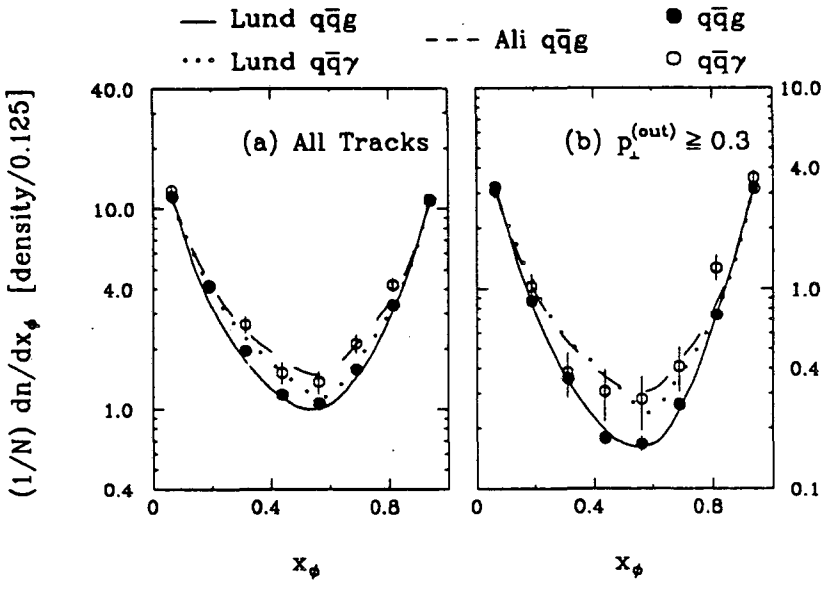

Figure 4.2 *The charged track density in the region between jets 1 and 2 versus the normalised angle x_ϕ. The densities are plotted (a) for all tracks and (b) for tracks with $p_\perp^{(out)} \geq 300$ MeV/c.*

enter the liquid argon calorimeter, and $E_\gamma \geq 2.2$ GeV. There are 1740 events in this Radiative Lund sample that pass our $q\bar{q}\gamma$ selection criteria and whose found photon jet is jet 3. The charged particle densities for these events reproduce the $q\bar{q}\gamma$ data over the full range of ϕ in both Figs. 4.1(a) and 4.1(b). Although not shown in the plot, we have generated a similar sample of Radiative Ali events using the same procedure. Both of these samples will be used throughout this chapter.

In order to look in more detail at the region between jets 1 and 2, we plot in Fig. 4.2

$$\rho(x_\phi) = \frac{1}{N}\frac{dn}{dx_\phi}$$

the charged particle density relative to x_ϕ, a normalized ϕ.[9] The variable x_ϕ is defined for tracks between jets 1 and 2 as ϕ_t/ϕ_2, where ϕ_t is the ϕ of the track and ϕ_2 is the ϕ of jet 2 (see Fig. 4.3). Using x_ϕ reduces systematic errors that might result from different jet angular distributions in our $q\bar{q}\gamma$ and $q\bar{q}g$ events. The depletion in the $q\bar{q}g$ data, and its enhancement by the $p_\perp^{(out)}$cut are clearly visible in these plots. The same Monte Carlo samples shown in Fig. 4.1 are also plotted in

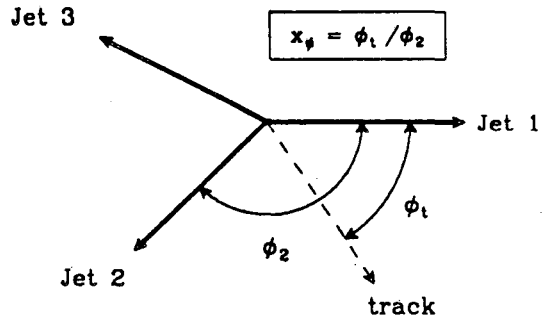

Figure 4.3 *Definition of the normalized event-plane angle x_ϕ.*

4.2, and again these models behave as expected.

A final method of presenting this data is shown in Fig. 4.4, where we plot the ratio of the charged track density distributions

$$r(x_\phi) \equiv \frac{\left[\frac{1}{N}\frac{dn}{dx_\phi}\right]_{q\bar{q}g}}{\left[\frac{1}{N}\frac{dn}{dx_\phi}\right]_{q\bar{q}\gamma}}$$

for all tracks and for tracks with $|p_\perp^{(out)}| \geq 300$ MeV/c. The ratio $r(x_\phi)$ depends only on the relative track densities in the two samples, and not on the absolute densities themselves. Therefore, as long as the two samples are affected equally, $r(x_\phi)$ will be insensitive to detector and event selection efficiencies and biases. Systematic differences between $\rho(x_\phi)$ for the two types of events should be small, because the events have such similar kinematics and topologies and because in this analysis the assignment of tracks to jets is only used to find jet energies. In Figs. 4.4(a) and 4.4(b), the ratio $r(x_\phi)$ is clearly different from one.

4.2 Systematic Errors

We have investigated possible contributions to $r(x_\phi)$ from detector and event selection biases in three ways. The first method uses our Ali Monte Carlo events, which should not exhibit the effects of QCD coherence. Naïvely, this is confirmed by Figs. 4.4(e) and 4.4(f), as the distributions shown for the Ali model are consistent

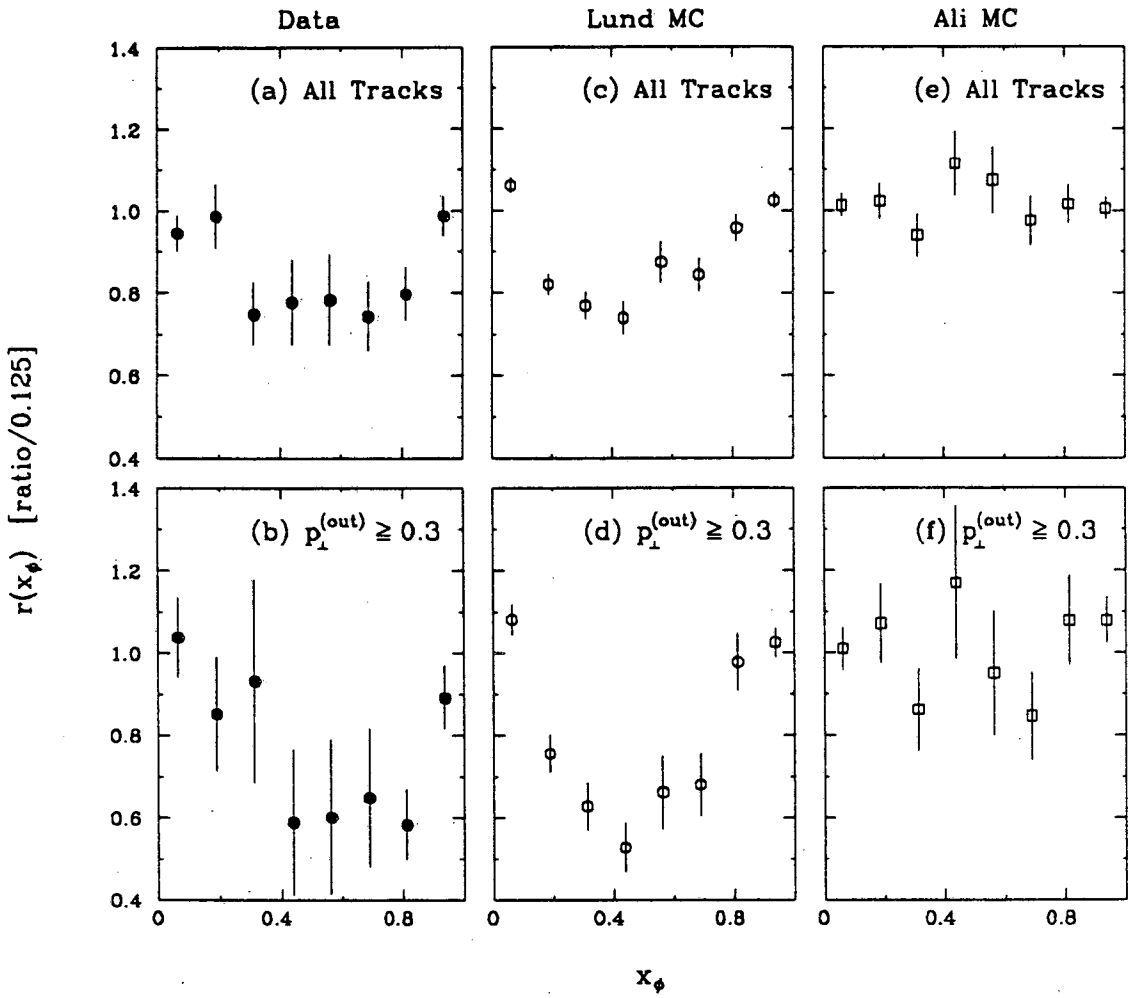

Figure 4.4 *The ratio of the charged track density from $q\bar{q}g$ events to the density from $q\bar{q}\gamma$ events, (a) for all tracks and (b) for tracks with $|p_\perp^{(out)}| \geq 300$ MeV/c. This ratio is also plotted for Lund Monte Carlo events in (c) and (d), and for Ali Monte Carlo events in (e) and (f).*

with $r(x_\phi) = 1$. For this comparison, we have used $q\bar{q}\gamma$ events selected from our Radiative Ali sample. However, this result is somewhat misleading, as $r(x_\phi)$ is consistent with one only because two subtle effects cancel. In the Ali model, gluon jets have a greater average multiplicity than quark jets. Because jets 1 or 2 are produced by the gluon jet 41% of the time, the track density between these jets will be somewhat higher for $q\bar{q}g$ events than for $q\bar{q}\gamma$ events. Secondly, fragmentation of $q\bar{q}\gamma$ events in this model correctly occurs in the rest frame of the q and $\bar{q}$, and the resulting hadrons are boosted back into the lab frame. The partons in $q\bar{q}g$ events,

however, are fragmented in the lab frame, and there is no boost. Particle density is enhanced in the direction of a boost, which in this case is the region between jets 1 and 2. The increase in the track density in $q\bar{q}\gamma$ events due to this boost cancels the increase in $q\bar{q}g$ events due to the higher multiplicity of gluon jets. Using the fact that we know which jet is the gluon jet in our Monte Carlo events, we can observe the size of the boost effect (see Figs. 4.5(a) and (b)) by comparing $q\bar{q}\gamma$ events with $q\bar{q}g$ events where the gluon jet is jet 3. According to QCD, hadrons are produced between the partons in both $q\bar{q}\gamma$ and $q\bar{q}g$ events by sources which are in motion in the lab frame (this will be shown in the next section). This boost effect, then, is an artifact of the fragmentation model.

To compare Ali events which do not suffer from these two effects, we have generated a sample of radiative Ali model events where the q and $\bar{q}$ are fragmented in the lab frame. When $q\bar{q}\gamma$ events from this No-Boost Ali sample are compared to Ali $q\bar{q}g$ events where the gluon jet is jet 3, $r(x_\phi)$ will equal one if no systematic differences exist between the two samples. As can be seen in Figs. 4.5(c) and 4.5(d), this is the case.

We have also checked for systematic errors in $r(x_\phi)$ by comparing Lund events as observed by the Mark II with the same events as observed by a perfect detector with exact track assignment to jets. The $r(x_\phi)$ distributions for our Lund events (with Mark II detector simulation) are shown in Figs. 4.4(c) and 4.4(d), and are consistent with those obtained from the data. These distributions are also plotted in Figs. 4.5(e) and 4.5(f), where they are compared with those obtained for the same events observed by a perfect detector. Detector and cluster-finding effects appear to introduce no significant systematic differences in the charged track densities of $q\bar{q}g$ and $q\bar{q}\gamma$ events.

Finally, as a cross-check, we have plotted $r(x_\phi)$ for our data and our Lund and Ali model events (see Fig. 4.6), where we have used method II to select the $q\bar{q}\gamma$ events. The error bars are larger in this plot because of the decreased statistics. Although $r(x_\phi)$ for the data in Fig. 4.6(a) is almost consistent with one, in

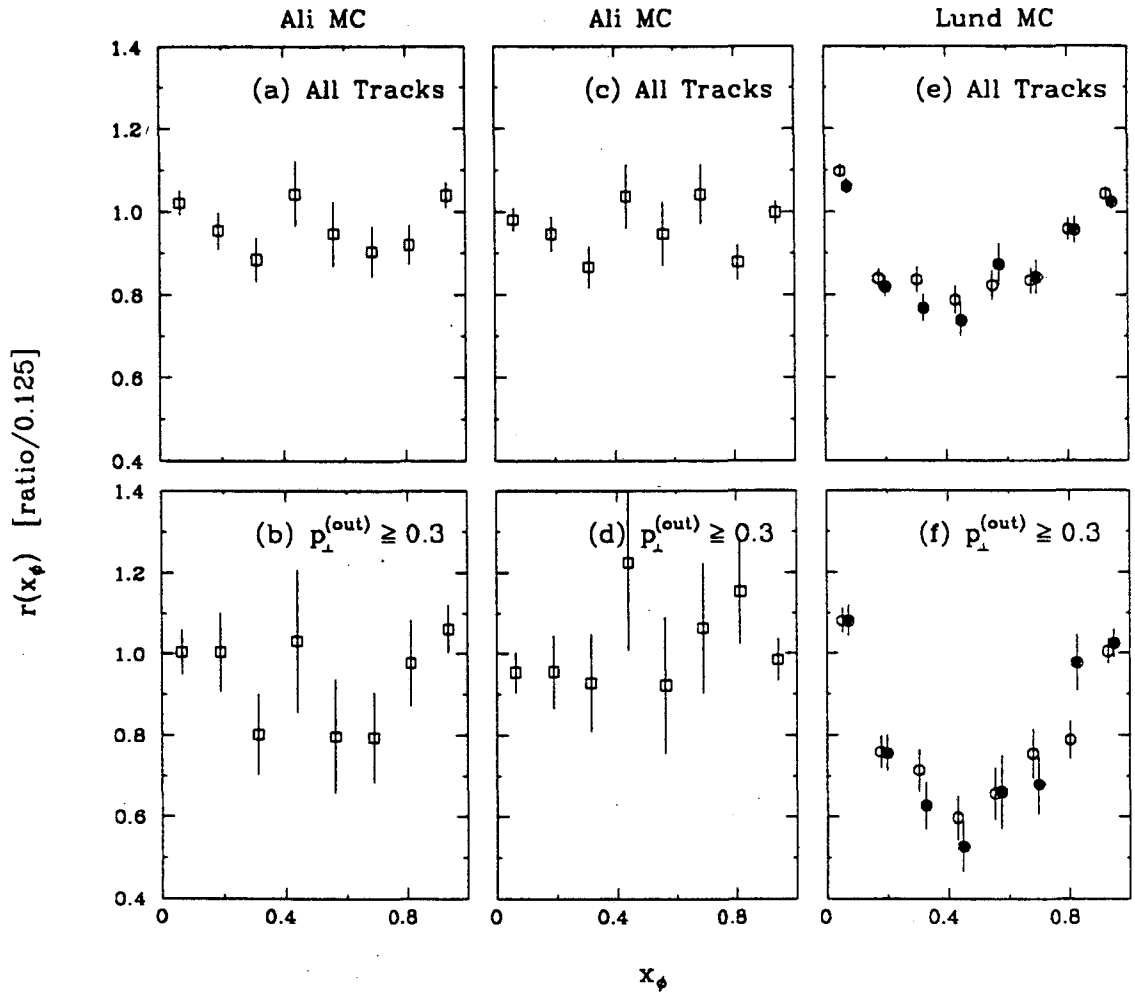

Figure 4.5 *The ratio $r(x_\phi)$ for (a)–(b) Ali events where jet 3 is the gluon jet in $q\bar{q}g$ events, (c)–(d) Ali events where jet 3 is the gluon jet in $q\bar{q}g$ events and radiative events are fragmented in the lab frame, and (e)–(f) Lund events as observed with an ideal detector (open circles) and with the Mark II (solid points).*

Fig. 4.6(b) the depletion is as deep as in Fig. 4.4(b). To test for systematic differences in the two samples, we compare method II $q\bar{q}\gamma$ events selected from our No-Boost Ali sample with Ali *3-jet* events where jet 3 is known to be the gluon jet. Shown in Figs. 4.6(e) and 4.6(f), $r(x_\phi)$ for this comparison does indicate a small systematic difference in the two samples. This difference arises from our method II selection procedure. Because tracks at large angles to the q and $\bar{q}$ jets and close to the photon are assigned to the photon jet, the found jet axes tend to be shifted slightly away from the photon. This reduces the angular region between the q and

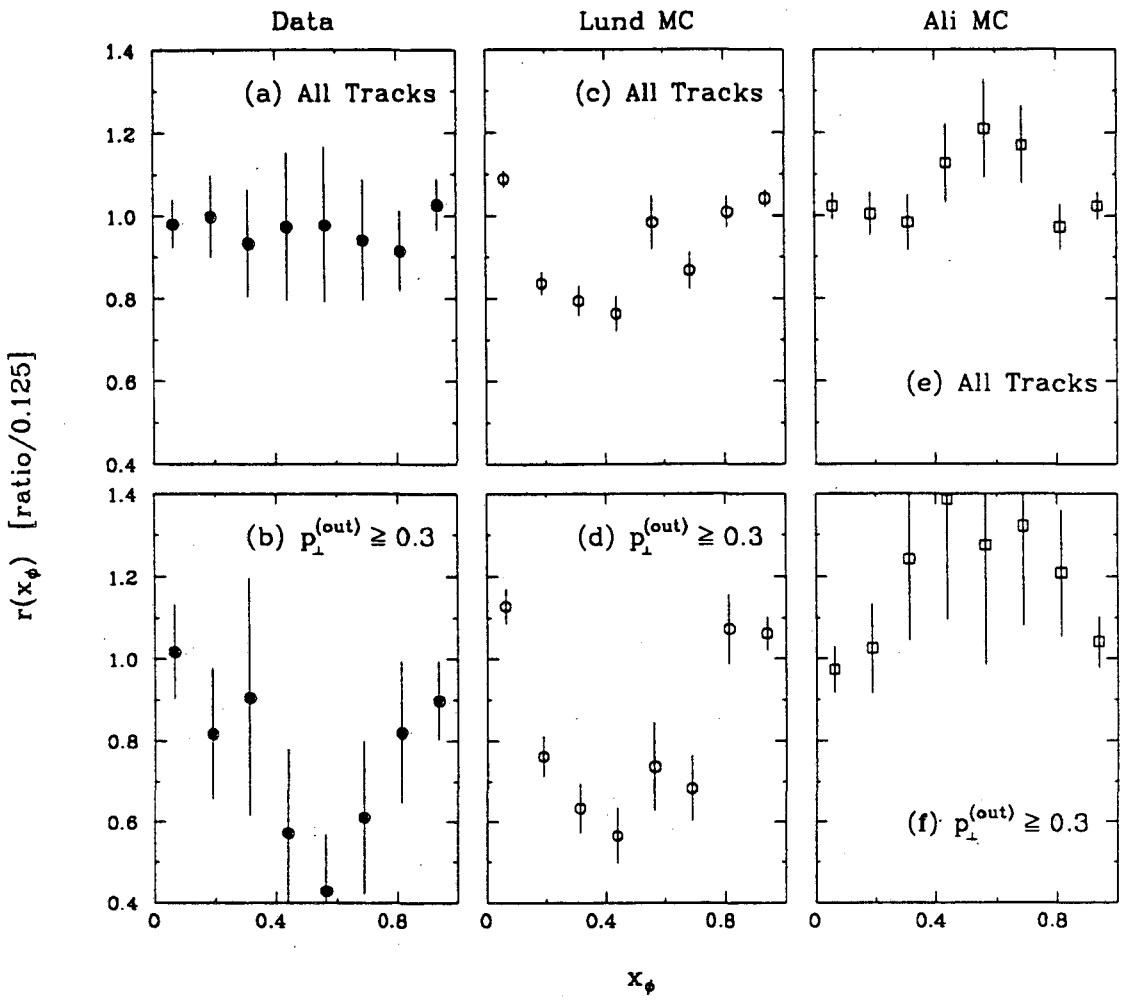

Figure 4.6 *The ratio $r(x_\phi)$ for our data, Lund model, and Ali model events when $q\bar{q}\gamma$ events are selected using method II.*

$\bar{q}$ jets, so that fewer tracks in the event tend to lie inside this region, decreasing the track density there. Even with this shift, however, our Lund Monte Carlo events still show a clear effect in Figs. 4.6(c) and 4.6(d). This fact, combined with the significant depletion in Fig. 4.6(b), leads us to believe that the result in Fig. 4.6(a) is a statistical fluctuation.

Systematic differences between our $q\bar{q}\gamma$ and $q\bar{q}g$ events therefore appear to be small, and cannot account for our observation that $r(x_\phi) \neq 1$. A clear difference in hadron density in the angular region between the q and $\bar{q}$ in $q\bar{q}\gamma$ and $q\bar{q}g$ events is demonstrated by the data, establishing that hard gluon emission influences particle

production on the side of the event plane opposite the gluon.

4.3 Comparison with Quantum Chromodynamics

To compare the predictions of QCD with our results, we need to merge (1.14) and (1.15) with the known differential cross-sections for $q\bar{q}g$ and $q\bar{q}\gamma$ production. This calculation has been done numerically with a computer program[35] which generates the relative event-plane angles of initial $q\bar{q}\gamma$ or $q\bar{q}g$ configurations, then calculates the probability of soft gluon emission in the regions between the partons. The results are shown in Fig. 4.7. No predictions are given in the regions near $\phi = 0°$, 150° and 235° in Fig. 4.7(a) because the calculations are not valid close to the partons in the event. The predictions have no absolute normalization, and the curves in Fig. 4.7(a) have been normalized so that the prediction for $q\bar{q}\gamma$ events (dashed line) approximately fits the data. The relative normalization of the $q\bar{q}\gamma$ and $q\bar{q}g$ curves is fixed by the calculation. There are curves from two slightly different QCD calculations for $q\bar{q}g$ events shown in Fig. 4.7, neither of which describes the *3-jet* data as well as the $q\bar{q}\gamma$ curve does the radiative *2-jet* data. This is especially true in the region $\phi > 150°$, where the calculations over-estimate the emission of soft gluons from jet 3. This is due to the fact that asymptotic QCD predicts that gluons are 9/4 times more likely to produce soft gluons than quarks, whereas this ratio has been shown to be consistent with 1.0 ($1.29^{+0.21}_{-0.41} \pm 0.20$) in 29 GeV *3-jet* events.[7] Because jets 1 and 2 are sometimes the gluon jet, QCD over-estimates the density in $q\bar{q}g$ events in the region between these two jets (see the dotted curve in Fig. 4.7(a)). The solid curve in Fig. 4.7(a) gives the result of the calculation for the case where jet 3 is always the gluon. Since this is true only 59% of the time, this prediction gives too large a depletion in the region between jets 1 and 2. These two curves, then, set upper and lower bounds on the true depletion in this region.

Predictions of the ratio $r(x_\phi)$ are given in Fig. 4.7(b). The two curves show the ratio of $q\bar{q}g$ and $q\bar{q}\gamma$ densities when all $q\bar{q}g$ configurations are included in the calculation (dotted curve) and when only configurations where the gluon jet is jet 3 are included (solid curve). In this plot, the actual normalization used for the curves

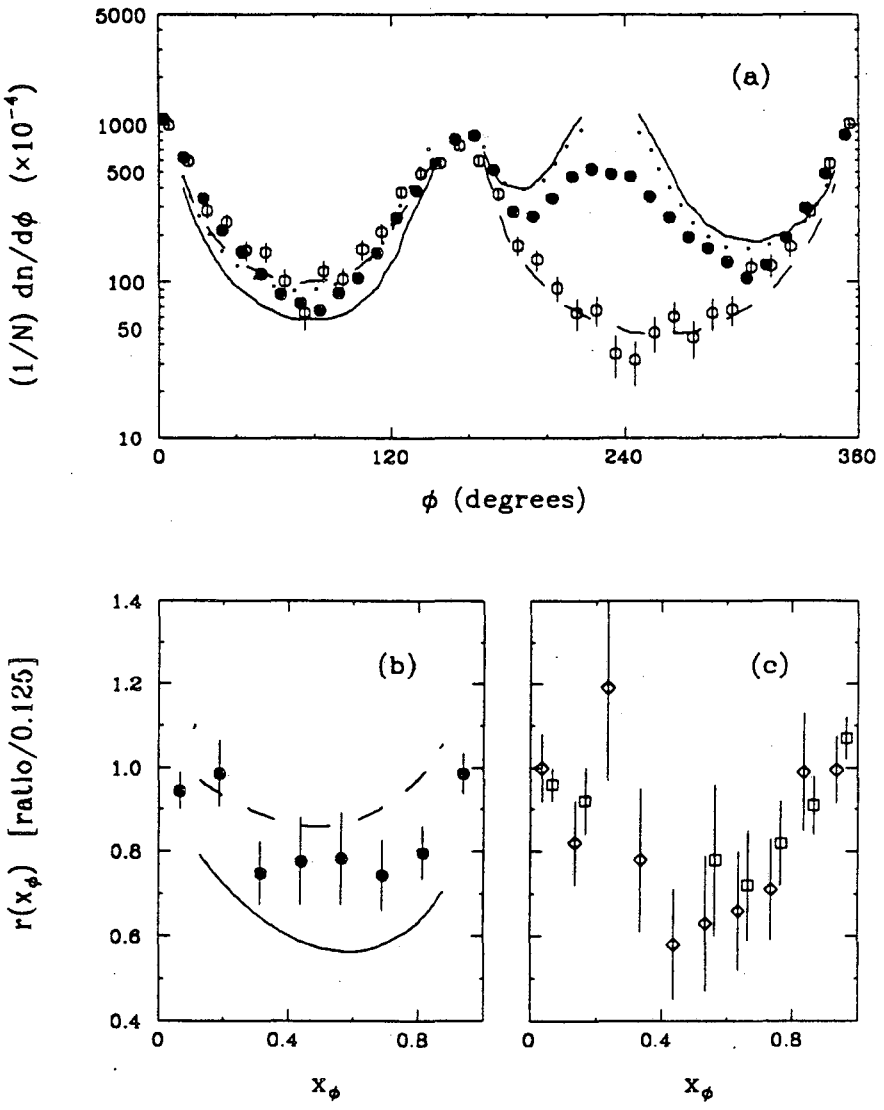

Figure 4.7 *Comparison of the charged particle density in the event plane for our data (points in (a) and (b)) and as predicted by the QCD calculations in Ref. 8 (curves). The calculations are not valid close to the partons in the events, and no predictions are given there. In (a), calculations are shown for $q\bar{q}\gamma$ events (dashed curves), $q\bar{q}g$ events (dotted curves) and $q\bar{q}g$ events in which the gluon is known to be jet 3 (solid curves). In (b), the dashed curve shows the ratio of the calculated densities for $q\bar{q}\gamma$ and $q\bar{q}g$ events, and the solid curve gives the ratio for $q\bar{q}\gamma$ and $q\bar{q}g$ (jet 3 = gluon jet) events. The squares and diamonds in (c) give the recently published results of Aihara et al. (Ref. 12).*

in Fig. 4.7(a) is not important, as it cancels out in the ratio. The data points lie well within the upper and lower bounds set by the two different calculations.

The comparison of our data and these calculations is interesting not only because it is a test of QCD, but because it provides insight into the production of final-state particles in hadronic events. Although these QCD calculations predict the soft gluon density between jets in hadronic events, our measurements are of the hadron density in the same regions. The fact that the shapes of these two different density distributions agree as well as they do implies that the soft gluons produce hadrons locally, so that these hadrons retain the density of the soft gluons.

We have recently published these findings.[11] Aihara *et al.* have also reported results from a similar analysis,[12] and their measurements of the ratio $r(x_\phi)$ are shown in Fig. 4.7(c). They report ratios for two different $q\bar{q}\gamma$ samples, those with an observed γ_{rad} (diamonds) and those where the γ_{rad} is not observed but escapes down the beam pipe (squares). The results from both of the experiments shown in Figs. 4.7(b) and 4.7(c) are in excellent agreement.

Chapter 5. Jet Properties

Jet properties do not scale with the energy of the jet. For example, significant scale breaking has been observed[26] in the inclusive charged-particle cross-section $s\,d\sigma/dx$ in e^+e^- hadronic events, where $x = p_{track}/E_{beam}$. In comparing gluon and quark jets, it is therefore important to use jets of similar energy. Differences in quark and gluon jets are expected because the color charge of the gluon is larger. Gluons should therefore fragment differently than quarks, producing jets which have a higher multiplicity, a softer momentum distribution and a larger opening angle than quark jets.[3,4]

Table 5.1 *Definition of our jet energy bins and gluon content of these bins for $q\bar{q}g$ events.*

x_{jet} *bin*	x_{jet} *range*	*Gluon Content*
(a)	$0.2 \leq x_{jet} < 0.4$	72%
(b)	$0.4 \leq x_{jet} < 0.6$	53%
(c)	$0.6 \leq x_{jet} < 0.8$	24%
(d)	$0.8 \leq x_{jet} \leq 0.9$	9%

5.1 METHOD

The energy spectrum of the q and g jets in our $q\bar{q}g$ and method II $q\bar{q}\gamma$ samples are displayed in Fig. 5.1. We use method II to select the $q\bar{q}\gamma$ events because the assignment of tracks to jets is important in this analysis. The spectra in Fig. 5.1 do not agree as well as those in Fig. 3.12 because photon jets from the $q\bar{q}\gamma$ sample are not included. To compare jets of similar energy, we divide the jets into the four energy bins listed in Table 5.1. The table also shows for each bin the expected fraction of the time that jets from $q\bar{q}g$ events are the gluon jet. More divisions are

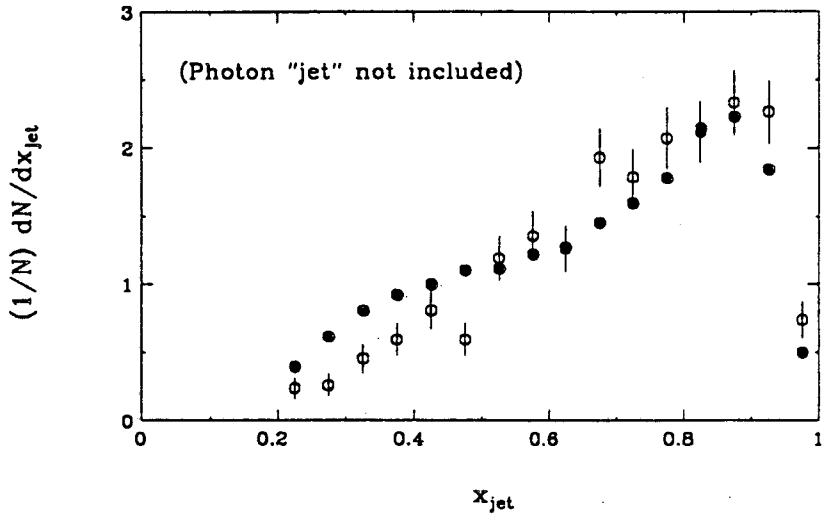

Figure 5.1 *The energy spectra of the q, $\bar{q}$ and g jets in our $q\bar{q}g$ (solid points) and method II $q\bar{q}\gamma$ (open points) events.*

not necessary because jet properties vary slowly with energy and because the jet energy spectra for the two samples are similar within each bin. Differences in gluon and quark jets should be most visible in bin (a), where the jets from $q\bar{q}g$ events are 72% gluon jets. The two highest energy bins have minimal gluon content, so these bins allow us to check for systematic differences in the measured properties of jets from the two samples.

Using charged tracks, we find momenta and multiplicity distributions for the jets in each energy bin. Distributions of the scaled momentum $x_p = p_{track}/E_{jet}$ are shown in Fig. 5.2. The momentum of a track perpendicular to its jet axis is divided into its components in and out of the event plane, $p_\perp^{(in)}$ and $p_\perp^{(out)}$. The distributions of these transverse momentum components are plotted in Figs. 5.3 and 5.4, respectively. Finally, Fig. 5.5 shows the distributions of the jet multiplicity n. Note that these distributions have not been corrected for detector acceptance.

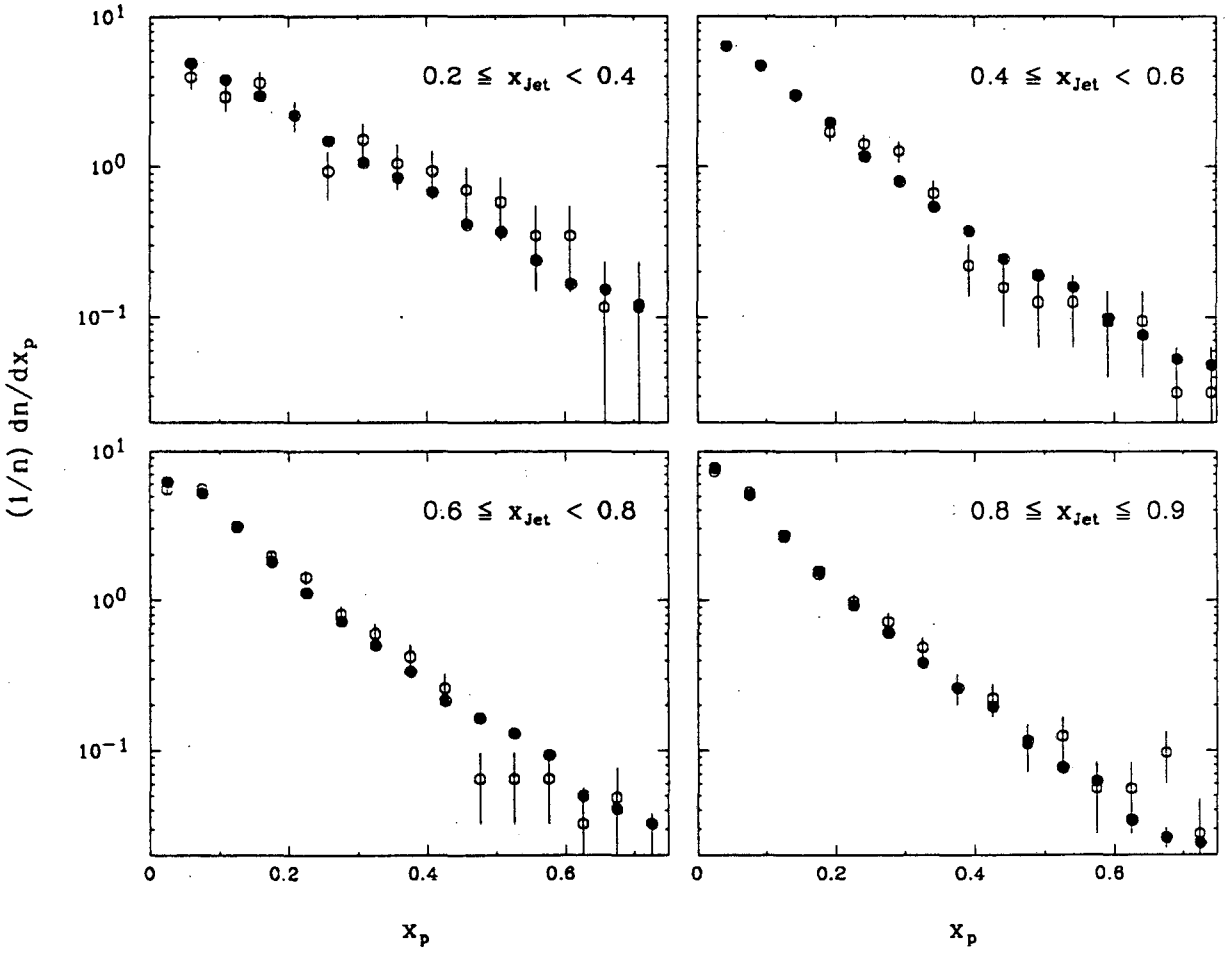

Figure 5.2 *The charged particle x_p distributions for jets from $q\bar{q}g$ (solid points) and method II $q\bar{q}\gamma$ (open points) events.*

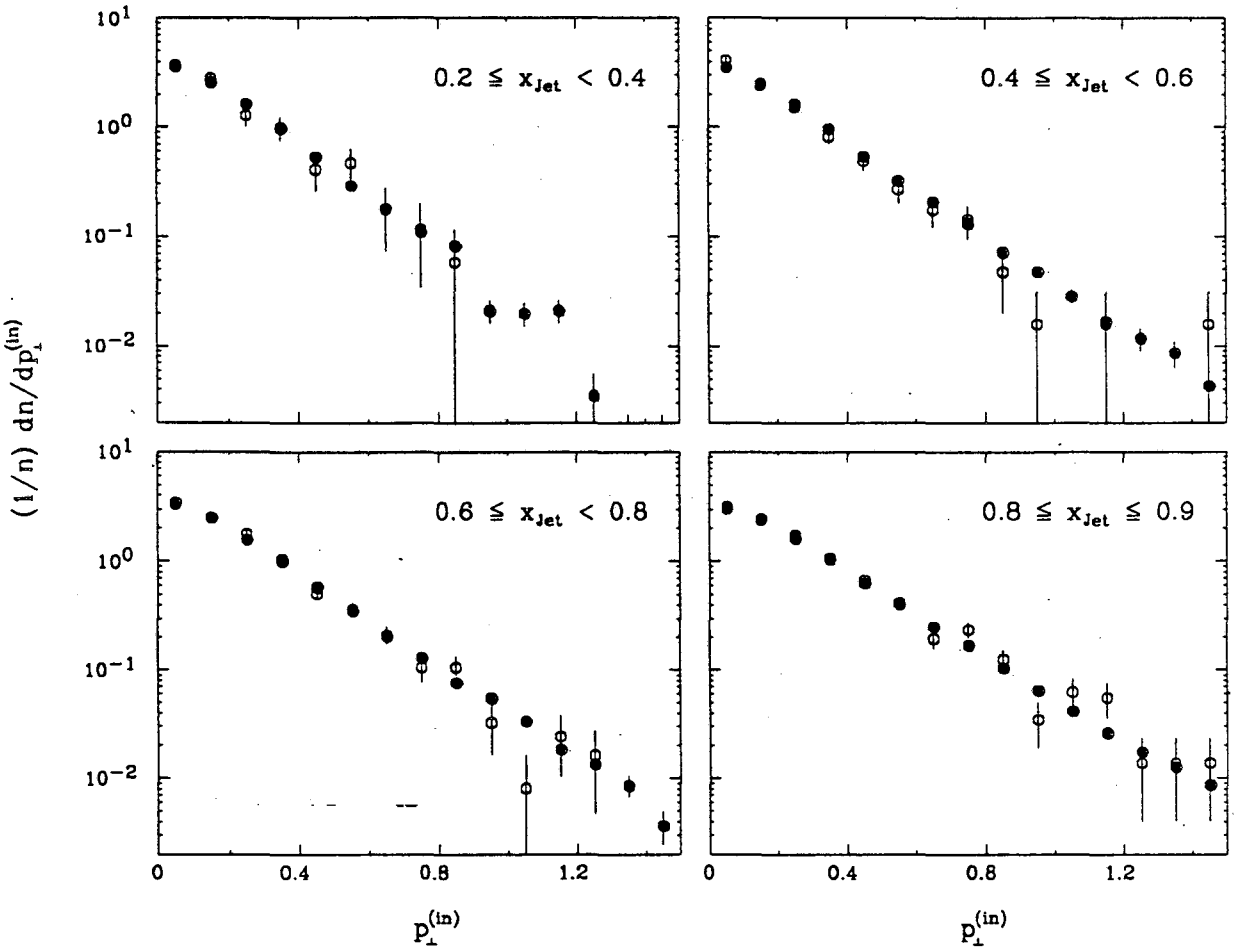

Figure 5.3 *The charged particle $p_\perp^{(in)}$ distributions for jets from $q\bar{q}g$ (solid points) and method II $q\bar{q}\gamma$ (open points) events.*

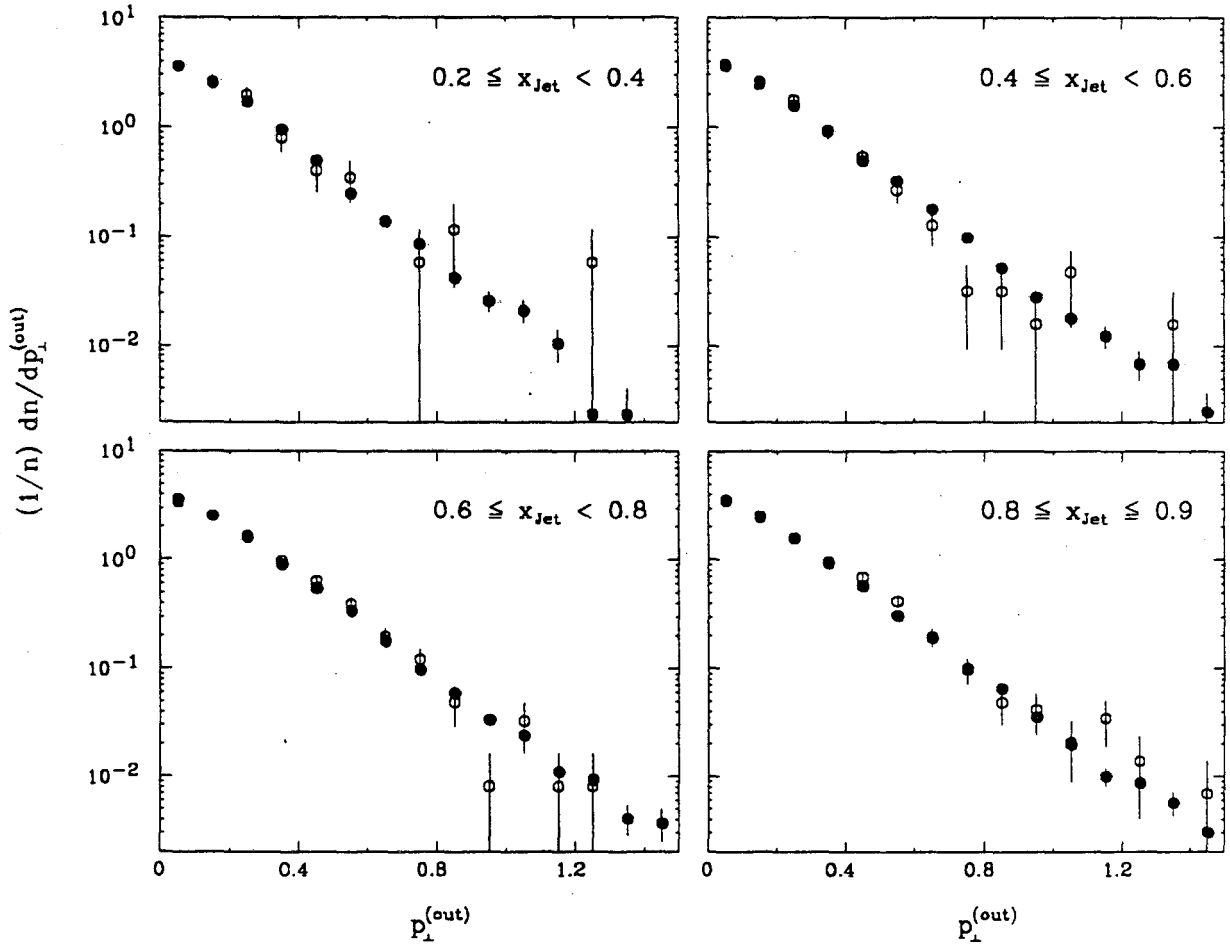

Figure 5.4 *The charged particle $p_\perp^{(out)}$ distributions for jets from $q\bar{q}g$ (solid points) and method II $q\bar{q}\gamma$ (open points) events.*

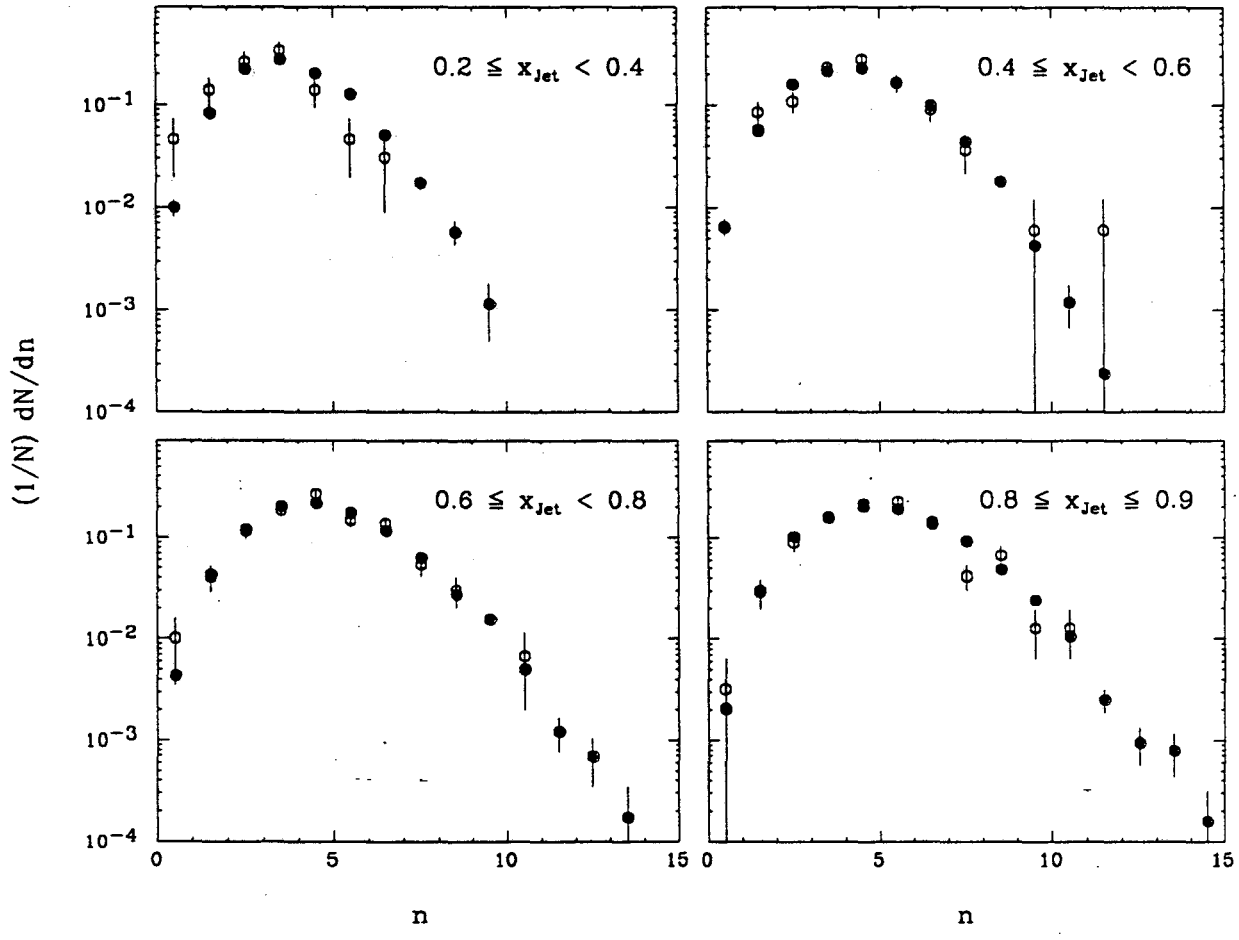

Figure 5.5 *The charged particle multiplicity (n) of jets from $q\bar{q}g$ (solid points) and method II $q\bar{q}\gamma$ (open points) events.*

5.2 SYSTEMATIC ERRORS

Before examining jet properties in more detail, we investigate possible systematic errors in our analysis. In the two highest jet-energy bins in Figs. 5.2–5.5, the distributions for jets from $q\bar{q}\gamma$ and $q\bar{q}g$ events are nearly identical. The averages of x_p, $p_\perp^{(out)}$, $p_\perp^{(in)}$and n for the jets in each energy bin are shown in Table 5.2. For jets in the two highest bins the averages agree well within the roughly 3% statistical errors given in Table 5.2. This suggests that if any systematic errors do exist in the lower jet-energy bins, they must be energy dependent.

To study such a possibility, we compare jets from our Radiative Ali sample of $q\bar{q}\gamma$ events with known quark jets from our Ali model $q\bar{q}g$ events. We use the Ali model because jets are fragmented independently in this model. Quark jets in Ali $q\bar{q}g$ and $q\bar{q}\gamma$ events should therefore be identical, which allows us to look for systematic errors caused by our selection procedure or by detector effects. The distributions of x_p, $p_\perp^{(in)}$, $p_\perp^{(out)}$and n for these two samples are shown in Figs. 5.6, 5.7, 5.8and 5.9, respectively, and their averages are given in Table 5.2. The distributions and averages for x_p, $p_\perp^{(in)}$and $p_\perp^{(out)}$ are in excellent agreement for all energy bins, typically differing by less than 5%. We therefore assign a 5% systematic error to these averages. However, there is an energy dependent bias in our jet multiplicity measurement. This bias occurs because of the track-assignment confusion of jets in $q\bar{q}g$ events. High energy jets have a larger multiplicity than low energy jets, and tracks are more likely to feed down into the low energy jets from the high energy ones. In our method II $q\bar{q}\gamma$ events, tracks are lost to but not gained from the photon jet, so when the photon jet is jet 1 this feed-down does not occur. As a result, low energy jets in our Ali $q\bar{q}\gamma$ sample have a slightly lower multiplicity than similar jets in our Ali $q\bar{q}g$ sample. This does not have a significant impact on our momentum distributions because very few tracks are affected in an event (about 0.5 track per event according to Table 5.2) and because these tracks have very low momenta.

Table 5.2 *Average momenta and multiplicities of the jets in each energy bin. The averages for the Ali model $q\bar{q}g$ events are for quark jets only. The errors shown are statistical only.*

Variable	*Bin*	Data		Ali MC	
		$q\bar{q}\gamma$	$q\bar{q}g$	$q\bar{q}\gamma$	$q\bar{q}g$
$\langle x_p \rangle$	(a)	0.224 ± 0.013	0.193 ± 0.002	0.203 ± 0.005	0.199 ± 0.004
	(b)	0.140 ± 0.005	0.141 ± 0.001	0.154 ± 0.002	0.142 ± 0.002
	(c)	0.124 ± 0.003	0.121 ± 0.001	0.126 ± 0.002	0.122 ± 0.001
	(d)	0.111 ± 0.004	0.108 ± 0.001	0.113 ± 0.002	0.109 ± 0.001
$\langle p_\perp^{(in)} \rangle$ [GeV/c]	(a)	0.192 ± 0.012	0.201 ± 0.002	0.184 ± 0.005	0.190 ± 0.004
	(b)	0.187 ± 0.007	0.209 ± 0.002	0.207 ± 0.003	0.199 ± 0.002
	(c)	0.213 ± 0.005	0.215 ± 0.001	0.224 ± 0.003	0.215 ± 0.001
	(d)	0.228 ± 0.007	0.227 ± 0.002	0.237 ± 0.003	0.224 ± 0.002
$\langle p_\perp^{(out)} \rangle$ [GeV/c]	(a)	0.191 ± 0.013	0.192 ± 0.002	0.191 ± 0.006	0.201 ± 0.005
	(b)	0.188 ± 0.007	0.198 ± 0.001	0.204 ± 0.003	0.201 ± 0.002
	(c)	0.209 ± 0.005	0.201 ± 0.001	0.214 ± 0.003	0.204 ± 0.001
	(d)	0.202 ± 0.006	0.200 ± 0.001	0.205 ± 0.003	0.201 ± 0.002
$\langle n \rangle$	(a)	2.65 ± 0.16	3.29 ± 0.03	3.09 ± 0.03	3.41 ± 0.07
	(b)	3.78 ± 0.12	3.87 ± 0.03	3.70 ± 0.05	3.94 ± 0.04
	(c)	4.14 ± 0.10	4.23 ± 0.02	4.27 ± 0.04	4.33 ± 0.03
	(d)	4.57 ± 0.14	4.52 ± 0.03	4.62 ± 0.06	4.66 ± 0.03

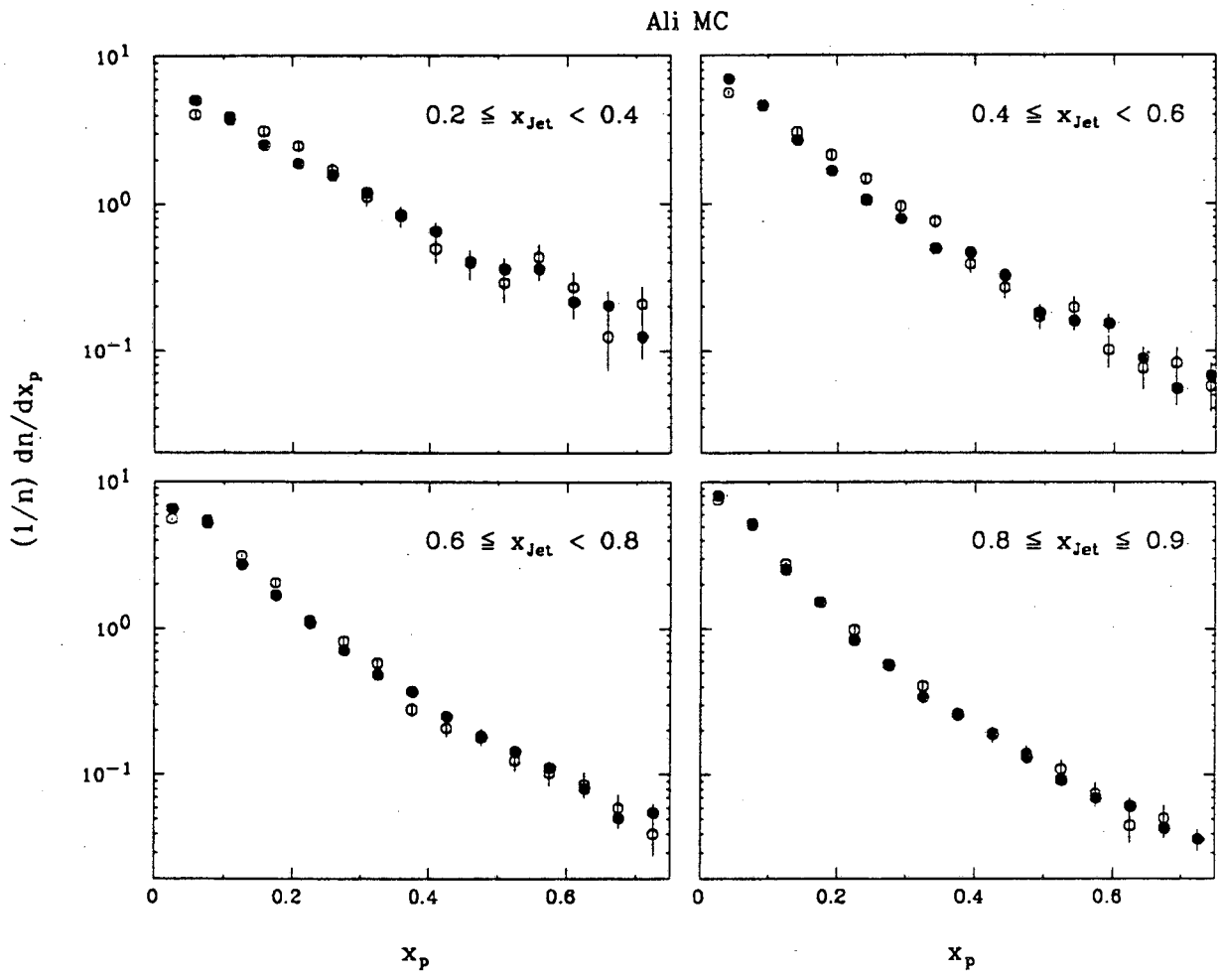

Figure 5.6 *The charged particle x_p distributions for the quark jets from Ali model $q\bar{q}g$ (solid points) and method II $q\bar{q}\gamma$ (open points) events. Gluon jets are not included.*

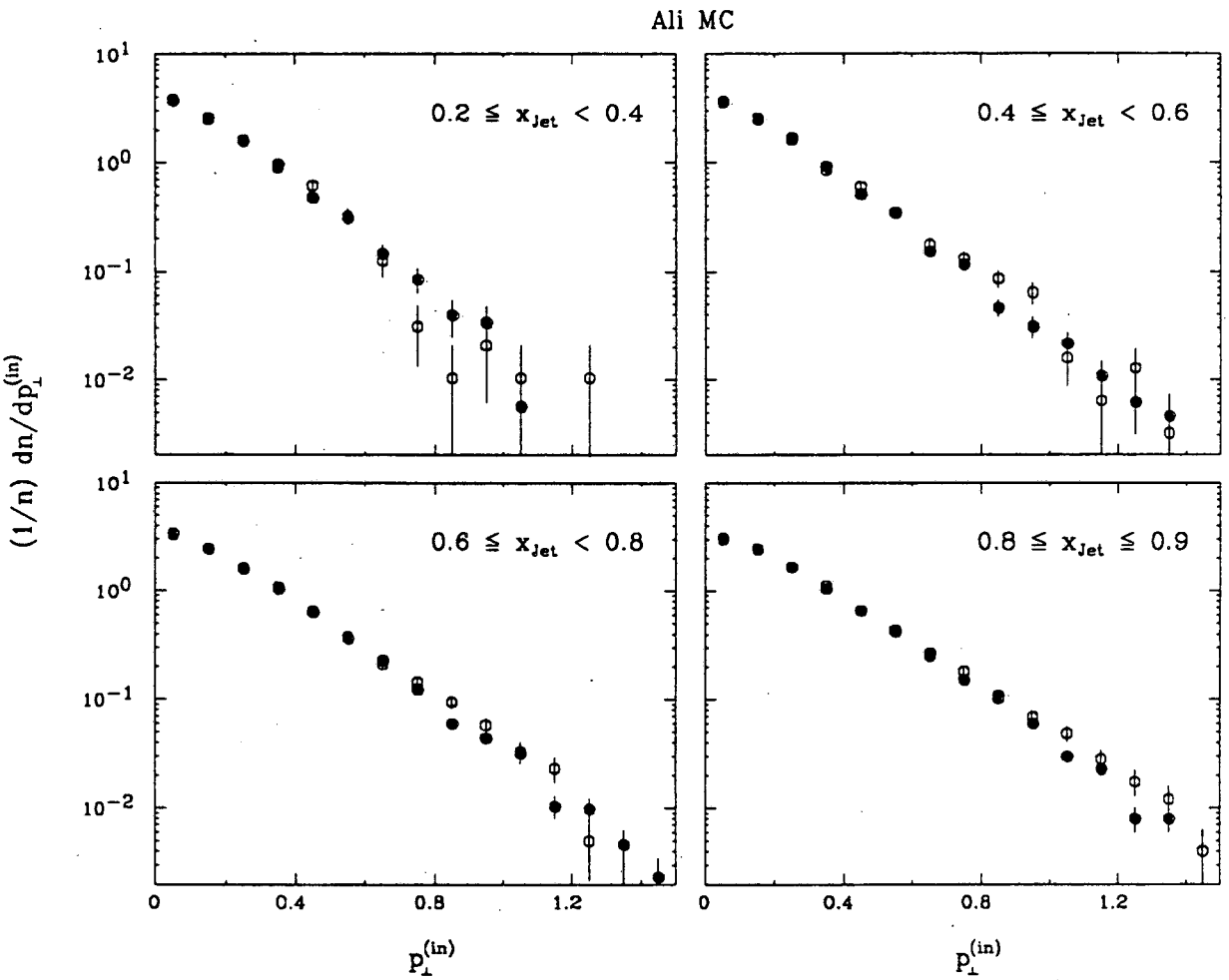

Figure 5.7 *The charged particle $p_\perp^{(in)}$ distributions for the quark jets from Ali model $q\bar{q}g$ (solid points) and method II $q\bar{q}\gamma$ (open points) events. Gluon jets are not included.*

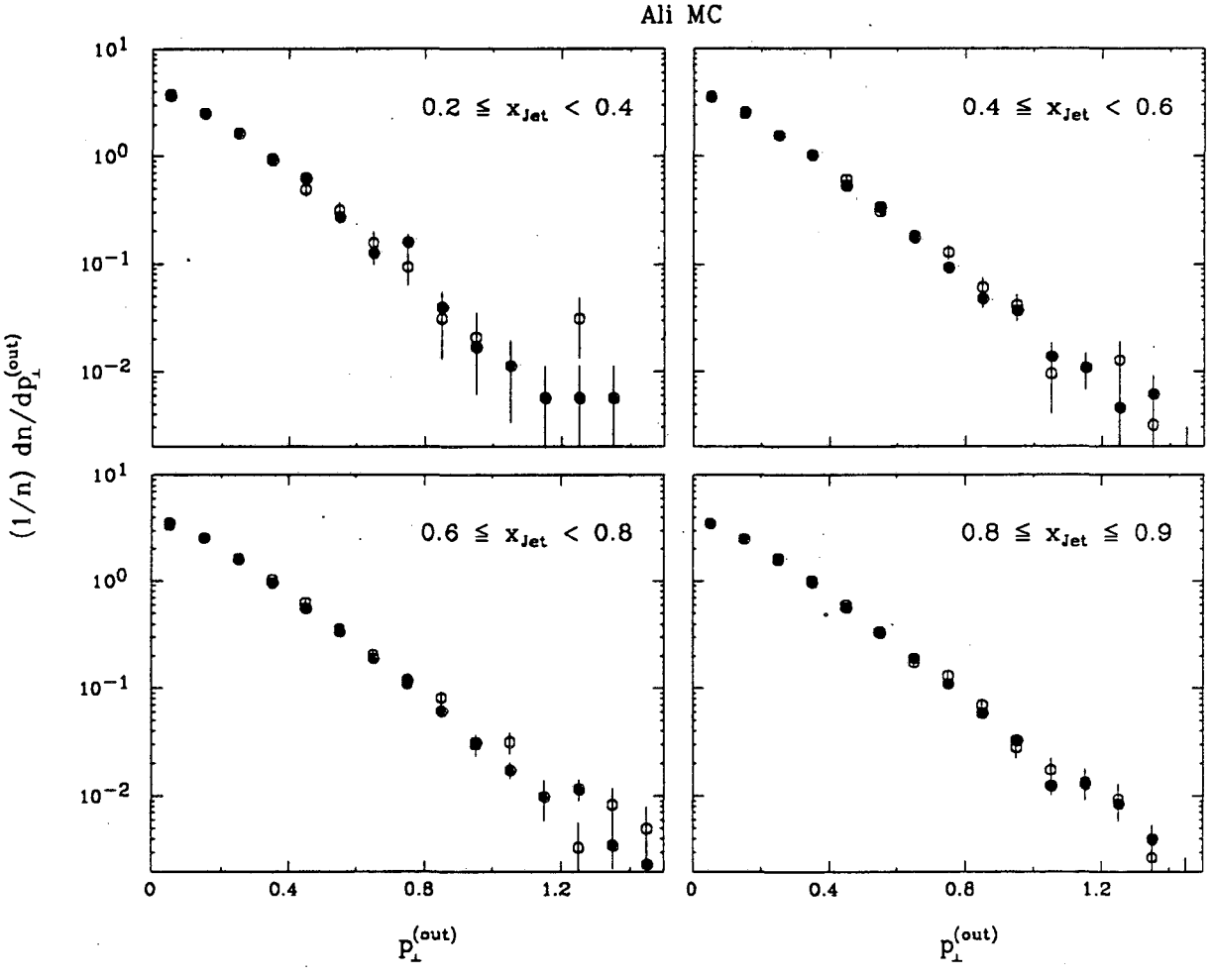

Figure 5.8 *The charged particle $p_\perp^{(out)}$ distributions for the quark jets from Ali model $q\bar{q}g$ (solid points) and method II $q\bar{q}\gamma$ (open points) events. Gluon jets are not included.*

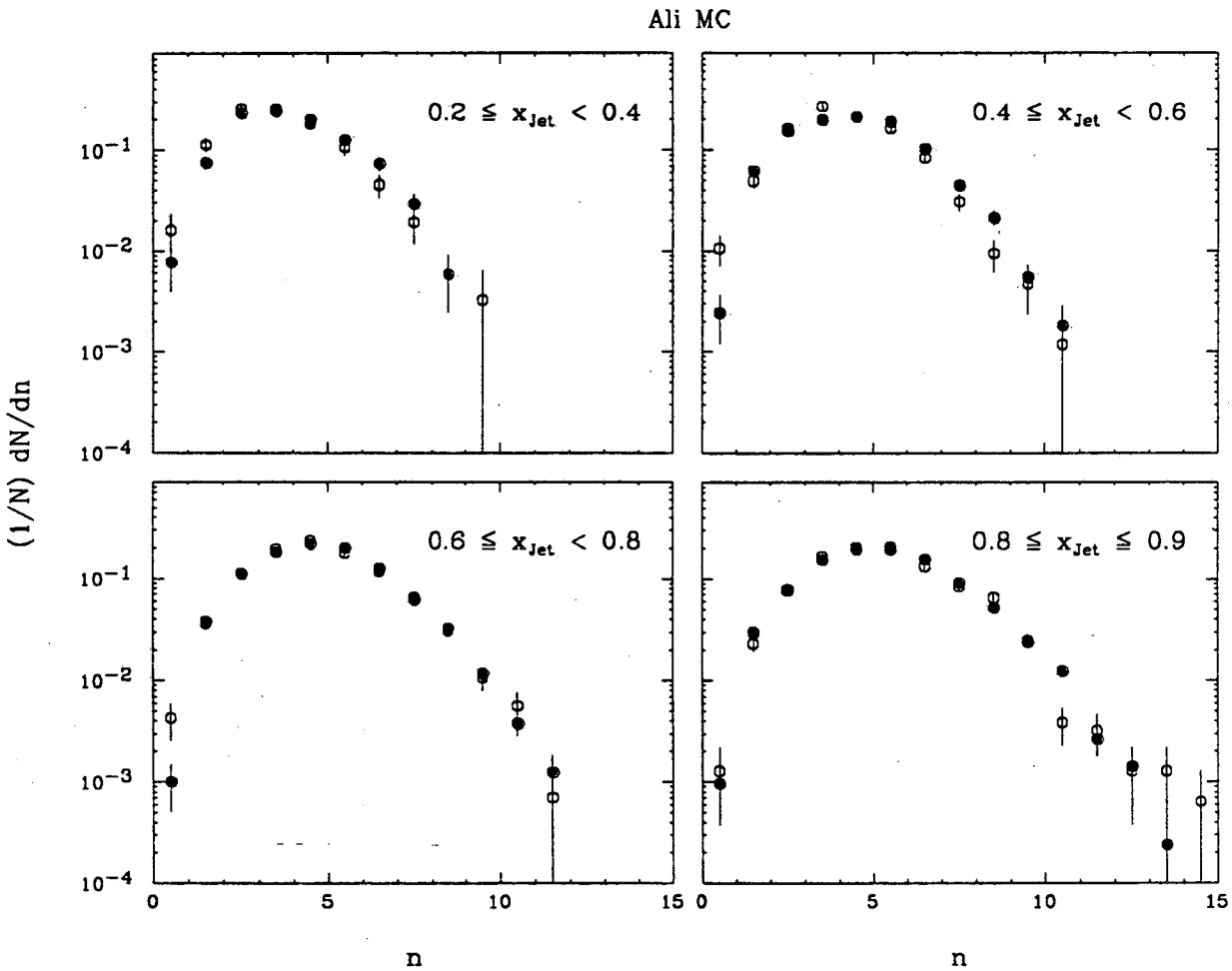

Figure 5.9 *The charged particle multiplicity (n) of the quark jets from Ali model $q\bar{q}g$ (solid points) and method II $q\bar{q}\gamma$ (open points) events. Gluon jets are not included.*

5.3 RESULTS

As is shown in the lowest jet-energy bin in Fig. 5.2, the x_p distribution for gluon jets is softer than for quark jets in our data. Because of our poor statistics, however, the difference is not conclusive. Adding a 5% systematic error to the statistical errors in Table 5.2, the averages of x_p for jets in this bin differ by a little more than two standard deviations. This is in agreement with previous studies,[5,6] which found a softer momentum distribution for gluon jets by comparing the third jet in *3-jet* events with jets from lower energy *2-jet* events. Bartel *et al.*[5] also compared jet 3 in *3-jet* events with equal energy second jets (*i.e.* jet 2) from other *3-jet* events in the same sample. In both of these previous studies, the jet energies were higher (6-10 GeV) than in this study (3-6 GeV).

No differences are observed in the $p_\perp^{(in)}$ and $p_\perp^{(out)}$ distributions and averages for gluon and quark jets. In bin (a), the averages of these quantities differ by less than 5%. Combining the statistical error of the averages for $q\bar{q}\gamma$ jets with a 5% systematic error, we should be sensitive to differences in these averages of 8% or more. Since 72% of the $q\bar{q}g$ jets in this bin are gluon jets, this corresponds to differences of 11% or more in gluon and quark jets. Bartel *et al.* found that gluon jets had larger values of $\langle p_\perp \rangle$ and $\langle p_\perp^{(out)} \rangle$ than quark jets, but it is possible that this result is not in conflict with ours since the average energy of the jets in bin (a) (4.5 GeV) is smaller than the average energy of the jets (8.0 GeV) that they were comparing. Looking at bin (b) in Table 5.2, where the average jet energy is about 7.5 GeV, there is a hint of a difference for $\langle p_\perp^{(in)} \rangle$ that would be in qualitative agreement with the results of Bartel *et al.*, but the statistical significance of the difference is not great (less than 2 standard deviations when systematic errors are included). Note that although the average opening angle of gluon jets is expected to be larger than in quark jets of the same energy, this does not imply a larger $\langle p_\perp \rangle$. If the x_p distribution is softer, the average opening angle of gluon jets will be larger even if $\langle p_\perp \rangle$ is the same as for quark jets.

Our data on gluon and quark multiplicities are inconclusive. It is expected that gluon jets will have a larger multiplicity, both from QCD and from our observation

that the gluon has a softer momentum distribution. The distributions for bin (a) in Fig. 5.5 and the averages in Table 5.2 do show a difference in the multiplicities, but it can probably be explained by the systematic error (discussed earlier) in this measurement at low jet energies. It is extremely unlikely, however, that the gluon to quark multiplicity ratio is 9/4 as predicted by asymptotic QCD. If all the multiplicity difference in bin (a) is assumed to be real, the ratio of the average multiplicities of $q\bar{q}g$ jets and $q\bar{q}\gamma$ jets is 1.24 ± 0.08, where the error is statistical only. If 70% of the $q\bar{q}g$ jets are gluon jets, QCD predicts that this ratio should be 1.88 in the asymptotic limit. Because the jets in bin (a) have an average energy of only 4.5 GeV, it is no surprise that our measurement of this ratio does not approach the asymptotic QCD limit. M. Derrick *et al.* found that 9.7 GeV gluon and quark jets had a multiplicity ratio of $(1.29^{+0.21}_{-0.41} \pm 0.20)$,[7] which supports our observation that the ratio is inconsistent with the asymptotic limit.

Chapter 6. Summary

By comparing *3-jet* and radiative *2-jet* events from e^+e^- annihilation, we have studied the local and global effects of the presence of a hard bremsstrahlung gluon in hadronic events. Accurate comparisons can be made because these two kinds of events have very similar kinematics and topologies, so that detector and event selection efficiencies and biases affect them almost equally.

Globally, we observe a depletion of hadrons in $q\bar{q}g$ events relative to $q\bar{q}\gamma$ events on the opposite side of the event plane from the gluon, in the angular region between the q and $\bar{q}$ jets. Quantum Chromodynamics (QCD) predicts that this effect is due to destructive interference of the soft gluon radiation from the initial quark, anti-quark and gluon in *3-jet* events, and the calculated magnitude of the effect is in agreement with our data. The QCD calculations are for the soft gluon density between the partons in the event, so this agreement implies a duality between these soft gluons and the hadrons in the events. The existence of a depletion demonstrates that the presence of a gluon significantly alters the color forces and hence the fragmentation process in hadronic events.

QCD predicts that gluon jets will have a softer momentum distribution, a wider opening angle and a higher multiplicity than quark jets. We have used $q\bar{q}\gamma$ and $q\bar{q}g$ events to compare low energy (4.5 GeV) gluon and quark jets. Our data indicate that gluon jets have softer x_p distributions than quark jets, while the transverse momentum distributions of these two types of jets are identical within our errors. Although we are unable to determine if the multiplicities of gluon (n_g) and quark (n_q) jets are different, the ratio $n_g/n_q = 9/4$ predicted asymptotically in QCD would not be consistent with our data.

Appendix A. Hadronic Event Generators

Although QCD is quite successful at predicting the total hadronic cross-section and the existence of gluon bremsstrahlung, it has so far been unable to describe the low Q^2, non-perturbative process by which partons fragment into hadrons. In order to test the perturbative predictions of QCD and to study hadronic events in e^+e^- annihilation, it is necessary to model the fragmentation process. There are currently three main classes of models in use: independent fragmentation (IF), string fragmentation, and QCD parton shower models. Brief descriptions of the first two are given below. Descriptions of QCD shower models can be found in the articles listed in Ref. 36.

A.1 Independent Fragmentation Models

The first model of hadron production by partons was the phenomenological scheme of Field and Feynman.[37] They described quark fragmentation as a recursive process, shown in Fig. A.1. The initial quark q_0 pulls a quark pair $\bar{q}_1 q_1$ from the vacuum, forming a hadron h_1 from the $q_0\bar{q}_1$ and leaving a new quark q_1. A fragmentation function $f(z)$ is used to determine how much of the initial quarks momentum $p(q_0)$ is carried off by h_1, so that $p(q_1) = (1-z)\,p(q_0)$. The quarks $\bar{q}_1$ and q_1 are produced with equal but opposite momentum $p_\perp$ transverse to the direction of q_0. This transverse momentum is determined by a gaussian distribution of width $\sigma_{p_\perp}$. Since fragmentation is a soft process, $\sigma_{p_\perp}$ is chosen to be of the order of the confining scale: $\sigma^2_{p_\perp} \sim (1\,\text{fermi})^2 \sim (350\text{MeV/c})^2$. The new quark q_1 and its successors fragment in the same way as q_0, until n hadrons are produced and a quark q_n of energy $E_n < E_{min}$ is left. If any of the hadrons produced by this process are unstable, they are decayed into secondary particles according to known branching fractions. Other parameters necessary to fully describe the process are the relative probability of pulling each flavor of quark from the vacuum, the fraction of vector

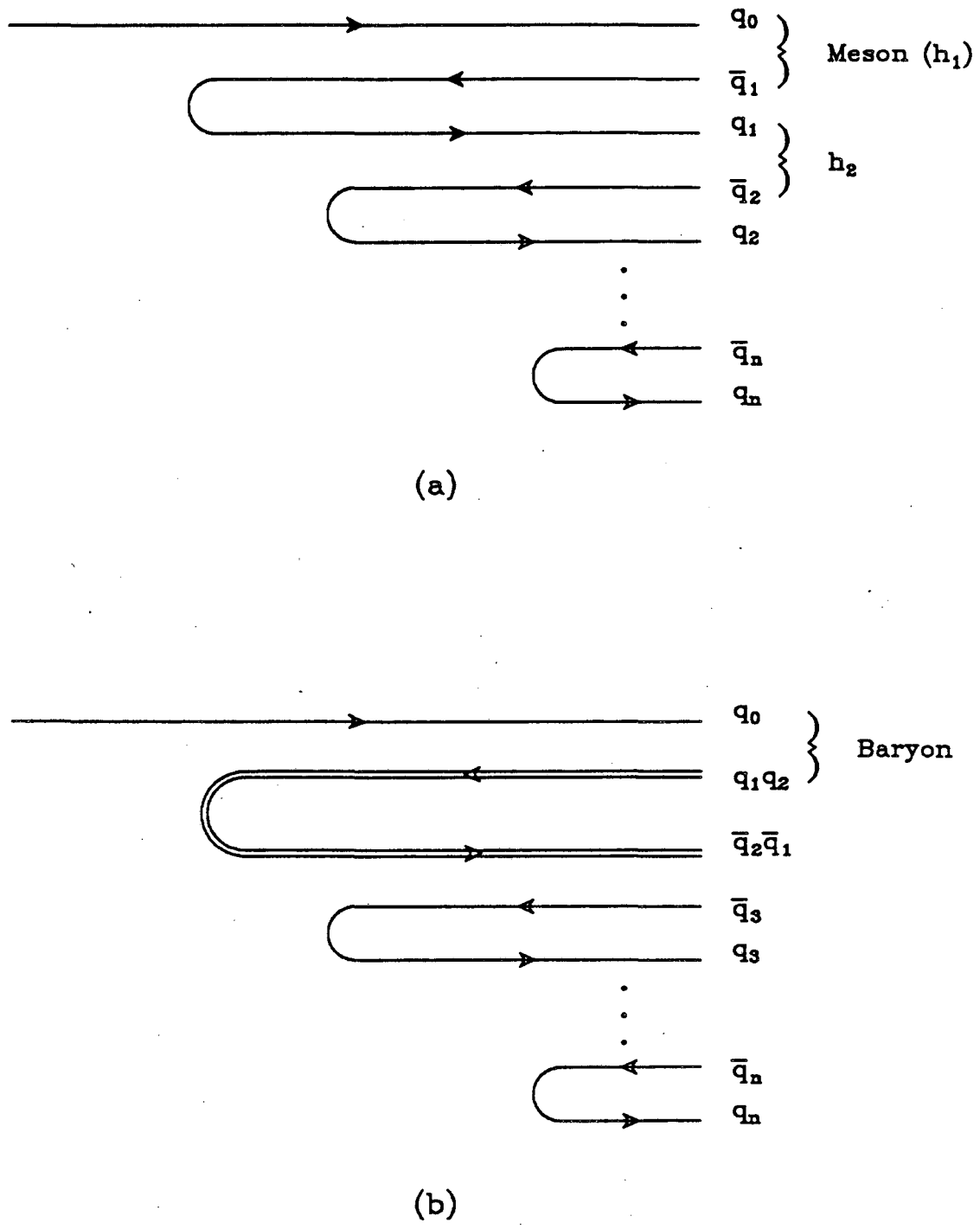

Figure A.1 *The Field-Feynman fragmentation scheme, described in the text. Baryon production in the scheme is illustrated in (b).*

particles produced relative to pseudoscalar particles, or the chance of pulling a "di-quark" pair $q_i q_j \bar{q}_j \bar{q}_i$ from the sea to produce baryons as in Fig. A.1(b).

The Field-Feynman scheme is used in the models of Hoyer *et al.*[38] and Ali *et al.*[30] to fragment partons produced by e^+e^- annihilations. After using QCD perturbation theory to produce a primordial $q\bar{q}$, $q\bar{q}g$, $q\bar{q}gg$ or $q\bar{q}q\bar{q}$ state, these models fragment each of the quarks and gluons independently. Gluons are split into a $q\bar{q}$ pair and fragmented. In the Hoyer model, all the gluon momentum is given to one of these quarks. Gluons therefore fragment like quarks, although different $f(z)$, $\sigma_{p_\perp}$, etc. may be chosen for gluons. In the Ali model, the quark pair shares the momentum of the gluon according to the Altarelli-Parisi splitting function[39] for $g \rightarrow q\bar{q}$. In both models, the leftover quarks from the Field-Feynman fragmentation chain are joined to form a low energy hadron.

A.2 Lund String Fragmentation

It is the confining color force between the initial $q\bar{q}$ pair in (1.1) that leads to the creation of hadrons as the q and $\bar{q}$ separate. The Lund string model[29] represents this force as a massless string stretching between the q and $\bar{q}$. The strong force is therefore modeled as a one-dimensional color flux tube, with the q and $\bar{q}$ acting as a flux source and sink. The tension in the string is proportional to the distance between the quark pair, with an energy density of $\kappa \simeq 1$ GeV/fermi. Hadrons are produced when enough energy is stored in the string to create a new $q\bar{q}$ pair between the original pair. The new q and $\bar{q}$ are also sources and sinks for the color flux and therefore break the string at the point at which they are produced. The string is broken so that the energy in each final string segment corresponds to the mass of a hadron formed by the $q\bar{q}$ pair at each of its ends, and so that the created hadron has a fraction z of the momentum of the string which is determined by a fragmentation function $f(z)$. Transverse momentum is again given to the created quark pairs with a gaussian distribution of width $\sigma_{p_\perp}$. Parameters similar to those in independent fragmentation models exist to control the vector/pseudoscalar, baryon/meson, and quark flavor production ratios. For

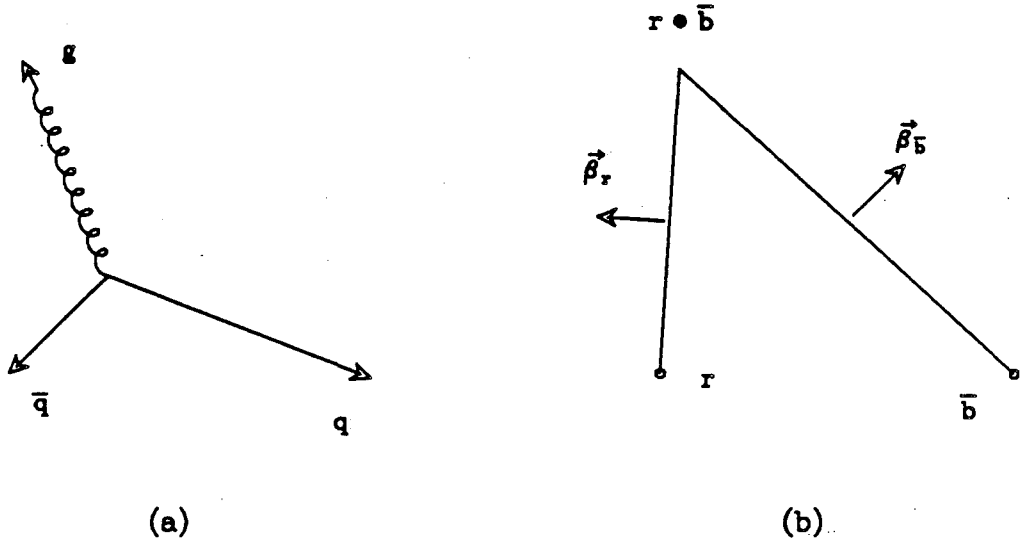

Figure A.2 *In the Lund picture, the gluon is a momentum carrying kink in the color flux string. The bent string in (b) shows the string corresponding to the $q\bar{q}g$ event shown in (a). Typical color charges of the partons are shown in (b). Note the change in color of the string at the kink.*

$q\bar{q}$ initial states, the string formalism and independent fragmentation schemes give very similar results. The Lund model does have fewer "technical" problems than IF models do. For example, energy and momentum are strictly conserved in the Lund model. This is not true in IF models.[40]

Major differences in string and IF fragmentation appear for events with three or more initial partons. Because gluons carry a color and an anti-color charge, their presence will modify the color flux in the event. The Lund model treats the gluon as a momentum carrying "kink" in the string. The color flux string stretches from the quark to the gluon, bends, and then stretches to the anti-quark, as shown in Fig. A.2. The kink essentially splits the string into two moving pieces, which fragment in their own rest frame. Hadrons are produced symmetrically about a string segment in its center-of-mass. The motion of the strings and the lack of a string segment between the q and $\bar{q}$ leads to a depletion of particles in this region. If one replaces the strings in the Lund model with the color dipoles of the QCD calculation described in Chapter 1, it is easy to see why the Lund model reproduces

the particle depletion between the q and $\bar{q}$ predicted by QCD. Although according to QCD there is a dipole in this region it can safely be ignored since it contributes only at the 10% level. The Lund assumption that particles are produced by two moving strings stretched between the q and g and the $\bar{q}$ and g is therefore a good one.

Appendix B. Monte Carlo Input Parameters

The values of the input parameters used when generating the Monte Carlo samples listed in Table 3.1 are given in the following tables. All samples created with the Ali model were generated using the parameters given in Table B.1, and all Lund samples were generated using the parameters shown in Table B.2. There were two different fragmentation functions used in the Ali model. For light quarks (u, d and s) the Field-Feynman[37] function

$$f_l(z) = 1 - a + a(r+1)(1-z)^r$$

was used, while for heavy quarks (c and b) we used the form of Peterson *et al.*[41]

$$f_H(z) = \left[z \left(1 - \frac{1}{z} - \frac{\epsilon}{(1-z)} \right)^2 \right]^{-1} .$$

In the Lund model the Lund symmetric fragmentation function[29]

$$f_s(z) = \frac{(1-z)^a}{z} \exp(-b m_\perp^2 / z)$$

was used. The transverse mass $m_\perp$ in $f_s(z)$ is defined in (1.17).

Table B.1 *Values used for the Ali model input parameters. The fragmentation functions for light (u, d and s) and heavy (c and b) quarks are denoted by $f_l(z)$ and $f_H(z)$, respectively. These functions are defined in the text.*

Ali Model Parameters	
Parameter	*Value*
thrust cut for 3-parton events	0.95
acoplanarity cut for 4-parton events	0.05
Λ_{QCD} (in GeV)	0.30
light quark vector fraction in fragmentation: P(spin 1)	0.58
charm quark vector fraction: P(spin 1)	0.75
strange quark fraction: $P(s)$	0.20
di-quark fraction: $P(q\bar{q})$	0.10
$\sigma_{p_\perp}$ (quarks)	0.30
$\sigma_{p_\perp}$ (quarks from gluons)	0.30
$\sigma_{p_\perp}$ (di-quarks)	0.36
r for light quarks in $f_l(z)$	0.75
a for light quarks in $f_l(z)$	1.00
r for di-quarks in $f_l(z)$	2.00
a for di-quarks in $f_l(z)$	1.00
ϵ for charm in $f_H(z)$	0.30
ϵ for bottom in $f_H(z)$	0.03

Table B.2 *Values used for the Lund model input parameters. The fragmentation function $f_s(z)$ is defined in the text.*

Lund Model Parameters	
Parameter	*Value*
y_{min} cut for 3, 4-parton events	0.02
Λ_{QCD} (in GeV)	0.50
light quark vector fraction in fragmentation: P(spin 1)	0.50
heavy quark vector fraction: P(spin 1)	0.75
di-quark vector suppression: P(spin 1)/P(spin 0)	0.05
strange quark suppression: $P(s)/P(d)$	0.30
di-quark suppression: $P(q\bar{q})/P(q)$	0.09
extra strange di-quark suppression: $(P(us)/P(ud))/(P(s)/P(d))$	0.35
$\sigma_{p_\perp}$	0.30
a in $f_s(z)$	1.00
b in $f_s(z)$	0.70

REFERENCES

1. R. Brandelik *et al.*, Phys. Lett. **86B**, 243 (1979);
   D. P. Barber *et al.*, Phys. Rev. Lett. **43**, 830 (1979);
   Ch. Berger *et al.*, Phys. Lett. **86B**, 418 (1979);
   W. Bartel *et al.*, Phys. Lett. **91B**, 142 (1980).
2. R. Brandelik *et al.*, Phys. Lett. **97B**, 453 (1980);
   Ch. Berger *et al.*, Phys. Lett. **97B**, 459 (1980);
   H. J. Behrend *et al.*, Phys. Lett. **110B**, 329 (1982).
3. S. J. Brodsky and J. F. Gunion, Phys. Rev. Lett. **37**, 402 (1976).
4. K. Shizuya and S. H. H. Tye, Phys. Rev. Lett. **41**, 787 (1978);
   M. B. Einhorn and B. G. Weeks, Nucl. Phys. **B146**, 445 (1978).
5. W. Bartel *et al.*, Phys. Lett. **123B**, 460 (1983) and Z. Phys. C **21**, 37 (1983).
6. A. Petersen *et al.*, Phys. Rev. Lett. **55**, 1954 (1985).
7. M. Derrick *et al.*, Phys. Lett. **165B**, 449 (1985).
8. Ya. I. Azimov, Yu. L. Dokshitzer, V. A. Khoze and S. I. Troyan, Phys. Lett. **165B**, 147 (1985).
9. W. Bartel *et al.*, Phys. Lett. **101B**, 129 (1981), and Phys. Lett. **134B**, 275 (1984).
10. H. Aihara *et al.*, Z. Phys. C **28**, 31 (1985);
    M. Althoff *et al.*, Z. Phys. C **29**, 29 (1985).
11. P. D. Sheldon *et al.*, Phys. Rev. Lett. **57**, 1398 (1986).
12. H. Aihara *et al.*, Phys. Rev.Lett. **57**, 945 (1986).
13. G. Kramer, *Theory of Jets in Electron-Positron Annihilation*, Springer Tracts in Modern Physics, Vol. 102 (Springer Berlin, Heidelberg, New York 1984).
14. G. Hanson *et al.*, Phys. Rev. Lett. **35**, 1609 (1975).
15. G. Wolf, *Proceedings of the 21st International Conference on High Energy Physics* (Paris 1982).
16. H. D. Politzer, Phys. Reports **14C**, 129 (1974);
    W. Marciano and H. Pagels, Phys. Reports **36C**, 137 (1978);

A. H. Mueller, Phys. Reports **73**, 237 (1981);
A. J. Buras, Rev. Mod. Phys. **52**, 199 (1980);
E. Reya, Phys. Reports **69**, 195 (1981);
G. Altarelli, Phys. Reports **81**, 1 (1982).

17. J. Ellis, M. K. Gaillard and G. G. Ross, Nucl. Phys. **B111**, 253 (1976) and Nucl. Phys. **B130**, 516 (1976).
18. T. Appelquist and H. Georgi, Phys. Rev. D **8**, 4000 (1973);
A. Zee, Phys. Rev. D **8**, 4038 (1973).
19. S. L. Wu, Phys. Reports **107**, 59 (1984).
20. M. Dine and J. Sapirstein, Phys. Rev. Lett. **43**, 668 (1979);
V. G. Chetyrkin, A. L. Kataev and F. V. Tkachev, Phys. Lett. **85B**, 277 (1979);
W. Celmaster and R. J. Gonsalves, Phys. Rev. Lett. **44**, 560 (1979).
21. The complete set of second-order diagrams is shown in Ref. 13.
22. F. A. Berends and R. Kleiss, Nucl. Phys. **B177**,237 (1981)
23. M. S. Gold, LBL-22433, Ph.D. Thesis (unpublished).
24. The approximate correction factor for final-state radiation, $(1+\alpha/\pi) = 1.002$, is similar in form to that given for gluon bremsstrahlung in (1.6). For more details, see Ref. 22.
25. B. R. Webber, Nucl. Phys. **B238**, 492 (1984).
26. J. Patrick *et al.*, Phys. Rev. Lett. **49**, 1232 (1982).
27. R. H. Schindler *et al.*, Phys. Rev. D **24**, 78 (1981);
G. S. Abrams *et al.*, IEEE Trans. Nucl. Sci. **27**, 59 (1980).
28. E. Fahri, Phys. Rev. Lett. **39**, 1587 (1977).
29. B. Andersson, G. Gustafson, G. Ingelman and T. Sjöstrand, Phys. Rep. **97**, 33 (1983).
30. A. Ali, E. Pietarinen, G. Kramer and J. Willrodt, Phys. Lett. **93B**, 155 (1980).
31. F. A. Berends, R. Kleiss and S. Jadach, Nucl. Phys. **B203**, 63 (1982) and

Computer Phys. Comm. **29**, 185 (1983).

32. See, for example, W. Bartel *et al.*, Z. Phys. C **25**,231 (1984).
33. T. Sjöstrand, Computer Phys. Comm. **28**, 229 (1983).
34. Tracks are assigned to jets using our knowledge of the fragmentation chain which produced the event and the direction vectors of the primordial partons.
35. The program used was a modified version of one written by Bryan Webber, and obtained directly from him. The program uses (1.5) to generate initial $q\bar{q}g$ states. To produce $q\bar{q}\gamma$ initial states, the radiative generator described in Ref. 31 was added to the original program.
36. R. D. Field and S. Wolfram, Nucl. Phys. **B213**, 65 (1983);
    G. Marchesini and B. R. Webber, Nucl. Phys. **B238**, 1 (1984);
    T. D. Gottschalk, Nucl. Phys. **B214**, Nucl. Phys. **B239**, 325 (1984), and Nucl. Phys. **B239**, 349 (1984).
37. R. D. Field and R. P. Feynman, Nucl. Phys. **B136**, 1 (1978).
38. P. Hoyer *et al.*, Nucl. Phys. **B161**, 349 (1979)
39. G. Altarelli and G. Parisi, Nucl. Phys. **B126**, 298 (1977).
40. For an interesting discussion of the repercussions of energy-momentum non-conservation in independent fragmentation models, see T. Sjöstrand, Z. Phys. C **26**, 93 (1984).
41. C. Peterson, D. Schlatter, I. Schmitt and P. M. Zerwas, Phys. Rev. D **27**, 105 (1983).

LAWRENCE BERKELEY LABORATORY
TECHNICAL INFORMATION DEPARTMENT
UNIVERSITY OF CALIFORNIA
BERKELEY, CALIFORNIA 94720